


## Superradiant emission stimulated by vortex-antivortex pair production in layered superconductors

Alex Gurevich<sup>✉\*</sup> and Ahmad Sheikhzada<sup>✉†</sup>*Department of Physics, Old Dominion University, Norfolk, Virginia 23529, USA* (Received 15 June 2024; revised 30 July 2024; accepted 1 August 2024; published 3 September 2024)

We report numerical simulations of coupled sine-Gordon and heat diffusion equations describing dynamic states stimulated by a trapped vortex driven by dc current in a stack of up to  $N = 321$  Josephson junctions. It is shown that the Cherenkov wake behind the vortex shuttle trapped in the stack can trigger proliferation of counterpropagating vortices and antivortices which get synchronized and form large-amplitude standing electromagnetic waves. This happens if the dc current density  $J$  exceeds a threshold value  $J_s$  which can be well below the Josephson interlayer critical current density  $J_c$  for underdamped junctions. The cavity modes stimulated by the vortex-antivortex pair production cause peaks in the radiated power  $P_N(J)$  with a nearly monochromatic spectrum at discrete values of  $J$  corresponding to the zero-field Fiske resonances. The power  $P_N(J)$  was evaluated for small rectangular stacks in the magnetodipole approximation and for large stacks in a single mode state. For small stacks, the highest peak in  $P_N(J)$  increases rapidly,  $P_N \propto N^6$ , with the number of junctions at  $N \leq 81$  and gradually slows down to  $P_N \propto N^2$  at  $161 \leq N \leq 321$ . For stacks larger than the radiation wavelength, we obtained  $P_N \propto N^5$  at  $N \lesssim 200$ – $300$  and  $P_N \propto N^2$  at larger  $N$ . At  $N \leq 321$  and representative parameters of  $\text{Bi}_2\text{Sr}_2\text{CaCu}_2\text{O}_{8+\delta}$ , we observed moderate overheating and no hotspots. The vortex-antivortex pair production can amplify THz radiation from  $\text{Bi}_2\text{Sr}_2\text{CaCu}_2\text{O}_{8+\delta}$  mesas for which trapping Josephson vortices could be used to stimulate THz emission at subcritical currents and optimize the radiation output.

DOI: [10.1103/PhysRevB.110.094501](https://doi.org/10.1103/PhysRevB.110.094501)

## I. INTRODUCTION

The intrinsic Josephson effect [1] in  $\text{Bi}_2\text{Sr}_2\text{CaCu}_2\text{O}_{8+\delta}$  (Bi-2212), in which the  $\text{CuO}_2$  planes sandwiched between the  $\text{Bi}_2\text{O}_2$  insulating layers form Josephson junctions (JJs), has caused much interest as a source of coherent radiation from the layered cuprates [2–6]. This effect can be used for the development of compact THz emitters and detectors for fundamental research and applications. Experiments on Bi-2212 mesas have revealed continuous radiation with powers  $\sim 1$ – $10^3$   $\mu\text{W}$  at 0.3–10 THz [3–6] and the appearance of hotspots in the mesas [7–13]. Such THz emitters can operate both at 4.2 K and 77 K [14,15].

The THz radiation from the JJ stack results from the excitation of collective modes of synchronized JJs [2–5]. Such modes can produce oscillating charge density at the edges of the stack and can be enhanced by electromagnetic coupling with surrounding structures [2–5] or mesa arrays [16,17]. Reaching higher radiation powers  $P_N$  requires better synchronization of JJs so that  $P_N$  would increase quadratically with the large number  $N$  of  $\text{CuO}$  planes in the crystal in a superradiant state. To improve the synchronization of JJs in Bi-2212 mesas it was proposed to use traveling electromagnetic (EM) waves [18–20], periodic inhomogeneity of the interlayer current density [21,22], in-plane magnetic fields [23], or currents [24].

In this paper we consider a mechanism of intrinsic synchronization of JJs and radiation stimulated by Cherenkov instability of a current-driven Josephson (J) vortex trapped in the stack [25]. Cherenkov radiation produced by moving vortex structures in JJ stacks is usually regarded as an extra contribution to the total radiation output [3,26]. Here we consider a nonlinear Cherenkov synchronization of JJs stimulated by a single vortex which triggers spontaneous production of vortex-antivortex (V-AV) pairs above a threshold current  $I_s$  in the absence of dc magnetic field. Such V-AV pair production has been observed in numerical simulation of single JJs [27,28], two and three-stacked JJs [29–32], annular JJs [33], JJ arrays [34,35], Josephson multilayers [25], and other systems described by coupled sine-Gordon equations [36,37]. This effect is most pronounced in underdamped JJ stacks in which the threshold current  $I_s$  can be well below the interlayer Josephson critical current  $I_c$ .

At  $I < I_s$ , a vortex trapped in an underdamped JJ stack bounces back and forth turning into antivortex upon each reflection from the edges of the stack [25]. At  $I > I_s$ , such a V-AV shuttle triggers proliferation of V-AV pairs which get synchronized and form a large-amplitude standing EM wave. Both the amplitude and the frequency of such resonant mode increase by orders of magnitude as compared to those of the V-AV shuttle at  $I < I_s$ . This mode causes oscillations of the magnetic moment and magnetodipole radiation from small JJ stacks with the emitted power  $P_N \propto N^6$  increasing rapidly with the number of JJs, as was shown by numerical simulations of up to 81 JJs [25]. Such strong increase of  $P_N$  with  $N$  mostly results from the increase of the number of produced V-AV pairs and the magnetic flux of a vortex

\*Contact author: [gurevich@odu.edu](mailto:gurevich@odu.edu)†Contact author: [sheikhzada.ahmad@gmail.com](mailto:sheikhzada.ahmad@gmail.com)

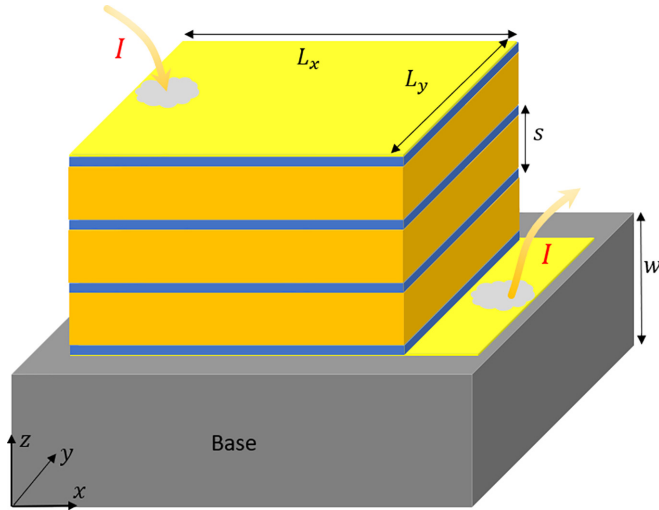


FIG. 1. Stack of intrinsic Josephson junctions (brown) between superconducting layers. A dc current  $I$  is injected from the top layer.

as the thickness of the stack increases. Extending these results to bigger stacks with  $N \gtrsim 10^2$ – $10^3$  typical of Bi-2212 mesas requires extensive numerical simulations to address the following questions. (1) How far can the strong increase of  $P_N \propto N^6$  with  $N$  continue and at what  $N$  could  $P_N$  eventually level off or start decreasing? (2) How much is  $P_N$  limited by overheating, which was disregarded in Ref. [25]? (3) How can the emission and its angular distribution change in mesas with lateral dimensions greater than the radiation EM wavelength  $\sim 10^{-1}$  mm at which the magnetodipole approximation is not applicable? In this work we address these issues by calculating  $P_N$  and the radiation spectrum for JJ stacks with up to 321 junctions.

The paper is organized as follows. In Sec. II we present the coupled sine-Gordon equations solved self-consistently with an equation for the mean temperature  $T$  of the JJ stack. A qualitative picture of a standing EM wave stimulated by a V-AV shuttle is given in Sec. III. Calculations of the magnetodipole radiated power  $P_N(\beta)$  as functions of the driving dc current and the number of layers for a single vortex trapped in the central JJ of a small stack are given in Sec. IV. In Sec. V we calculate  $P_N(\beta)$  for one trapped vortex in each JJ. In Sec. VI we evaluate the radiated power caused by a resonant mode in a rectangular JJ stack of arbitrary dimensions. Section VII concludes with a discussion of the results.

## II. MAIN EQUATIONS

In this work we solve numerically generic sine-Gordon equations [1–5,38–44], which describe dynamic states of a stack of  $N$  coupled JJs shown in Fig. 1:

$$\theta_n'' = [1 - \zeta(T)\Delta_d][\alpha_J(T)\sin\theta_n + \eta\dot{\theta}_n + \ddot{\theta}_n], \quad (1)$$

$$b_n = [1 - \zeta(T)\Delta_d]^{-1}\theta_n'. \quad (2)$$

Here  $\theta_n(x, t)$  is the phase difference across the  $n$ th junction,  $b_n = B_n(x, t)/B_0$  the dimensionless magnetic field parallel to the layers,  $B_0 = \mu_0 J_c \lambda_{c0} = \phi_0/2\pi s \lambda_{c0}$ ,  $\lambda_c$  and  $\lambda$  are the penetration depths of the parallel magnetic field  $\mathbf{B}$  along and

across the layers, respectively,  $\lambda_{c0} = \lambda_c(T_0)$ ,  $s$  is the spacing between the layers,  $\phi_0$  is the magnetic flux quantum,  $\Delta_d f_n \equiv f_{n+1} + f_{n-1} - 2f_n$  is the lattice Laplacian,  $J_c$  is the Josephson critical current density,  $\eta = \sigma_c \lambda_{c0}/c\epsilon_0\sqrt{\epsilon_c}$  is a damping parameter,  $\sigma_c$  is the interlayer quasiparticle conductivity,  $\epsilon_0$  and  $\mu_0$  are the vacuum electric and magnetic permittivities, the prime and overdot denote partial derivatives with respect to the dimensionless coordinate  $x/\lambda_{c0}$  and time  $t\omega_{J0}$ , respectively,  $\omega_{J0} = c/\sqrt{\epsilon_c}\lambda_{c0}$  is the Josephson plasma frequency at  $T = T_0$ ,  $c$  is the speed of light, and  $\epsilon_c$  is the dielectric constant along the crystal  $c$  axis. We consider one-dimensional (1D) solutions  $\theta_n(x, t)$  and  $b_n(x, t)$  independent of  $y$  and disregard the effects of charge imbalance [44] and in-plane quasiparticle currents [6,45] in Eqs. (1) and (2).

At the edges of the stack we imposed the boundary condition  $\theta_n'(0) = \theta_n'(L_x) = 0$  of zero in-plane super current density. Other boundary conditions account for a dimensionless dc uniform current density  $\beta = J/J_c(T_0)$  injected through the top JJ ( $n = 1$ ) and collected from the bottom JJ ( $n = N$ ) [41–43]. These boundary conditions were incorporated in the matrix Eqs. (1) and (2), which were solved numerically using the method of lines [46,47] as described in Appendix A.

The parameters  $\alpha_J(T)$  and  $\zeta(T)$  take account of dependencies of  $J_c(T)$  and  $\lambda(T)$  on the JJ temperature  $T(J)$ ,

$$\alpha_J = \frac{J_c(T)}{J_c(T_0)}, \quad \zeta = \frac{\lambda^2(T)}{s^2}, \quad (3)$$

where  $\zeta(T)$  quantifies the inductive coupling of the layers. We use  $J_c(T)$  for SIS junctions and an interpolation formula for  $\lambda(T)$  in Bi-2212 single crystals [10,48]:

$$J_c(T)/J_c(0) = 1 - (T/T_c)^2, \quad (4)$$

$$\lambda^2(0)/\lambda^2(T) = [1 - (T/T_c)^6](1 - 0.6T/T_c). \quad (5)$$

A mean temperature of the JJ stack  $T(J)$  is calculated self-consistently by solving Eqs. (1) and (2) and a stationary heat diffusion equation. As shown in Appendix B,  $T(J)$  in a thin JJ stack of thickness  $d$  on a base of thickness  $w \gg d$  is determined by the equation

$$\frac{1}{w} \int_{T_0}^T \kappa_c(T) dT = \frac{\hbar J_{c0}}{2et_a L_x} \sum_{n=1}^N \int_{t_0}^{t_0+t_a} dt \times \int_0^{L_x} [\eta\dot{\theta}_n^2 + \alpha_J\dot{\theta}_n \sin\theta_n] dx, \quad (6)$$

where  $\kappa_c(T)$  is the thermal conductivity of the base along the  $c$  axis. The right-hand side of Eq. (6) is the power generated per unit area of the stack. In our simulations  $t_0 = 2000$  was chosen to be larger than the transient time after which the steady-state solutions  $\theta_n(t)$  set in and  $t_a = 200$  is an averaging time to calculate steady-state  $T(\beta)$  and the radiation power.

Simulations start at a small current  $\beta \ll 1$  and run until a steady state  $\theta_n(t)$  was reached at  $t > t_0$ . Then these solutions were used to calculate  $T(\beta)$  in Eq. (6) and update  $\zeta(T)$  and  $\alpha_J(T)$  in Eqs. (1) and (2) for the next step  $\beta + \Delta\beta$ , where  $\Delta\beta \leq 0.01$ . In this way Eqs. (1)–(6) were solved iteratively for a sequence of driving currents  $\beta_{i+1} = \beta_i + \Delta\beta$  using  $\theta_n(t, \beta_i)$  obtained at the preceding  $i$ th step as initial conditions for Eqs. (1) and (2) at the  $(i + 1)$ th step and to update  $T(\beta_i)$  in

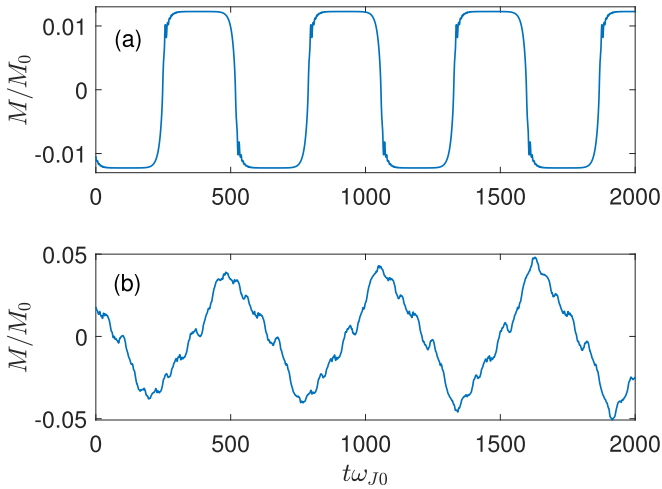


FIG. 2. Temporal oscillations of a magnetic moment  $M(t)$  due to reflections of vortices and antivortices from the edges at  $\eta = 0.1$ . (a)  $M(t)$  caused by a single vortex trapped in a central JJ at  $\beta = 0.585 < \beta_s$ ; (b)  $M(t)$  caused by a bouncing flux structure with one vortex per layer at  $\beta = 0.52 < \beta_s$ .

Eq. (6). For the input material parameters, we took  $T_c = 85$  K,  $\epsilon_c = 12$ ,  $s = 1.5$  nm,  $J_c(T_0) = 200$  A/cm<sup>2</sup>,  $\lambda(0) = 260$  nm,  $\lambda(T_0) = 264$  nm in a Bi-2212 crystal at the ambient temperature  $T_0 = 4.2$  K,  $\lambda_{c0} = 295$   $\mu$ m,  $\omega_{J0} = 0.29$  THz,  $L_x = \lambda_{c0}$ , and the base thickness  $w = 30$   $\mu$ m. The temperature dependence of  $\eta(T)$  was disregarded and  $\kappa_c(T) = \kappa_0(T/T_0)^a$  with  $\kappa_0 = 0.32$  W/mK and  $a = 0.67$  [10] was used.

### III. RESONANT MODES STIMULATED BY A VORTEX SHUTTLE

We start with an overview of the physics of the V-AV pair production by a moving vortex trapped in a stack with 21 JJs. This case was considered in Ref. [25] in a model

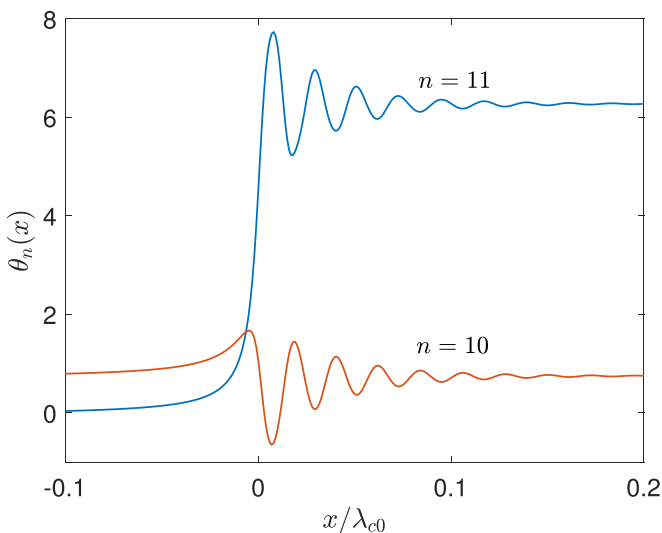


FIG. 3. Phase profile of a vortex propagating along a long central junction ( $n = 11$ ,  $L_x \gg \lambda_{c0}$ ) and the trailing tail of Cherenkov radiation on the neighboring JJ ( $n = 10$ ) calculated from Eq. (1) at  $\eta = 0.1$  and  $\beta = 0.685$ .

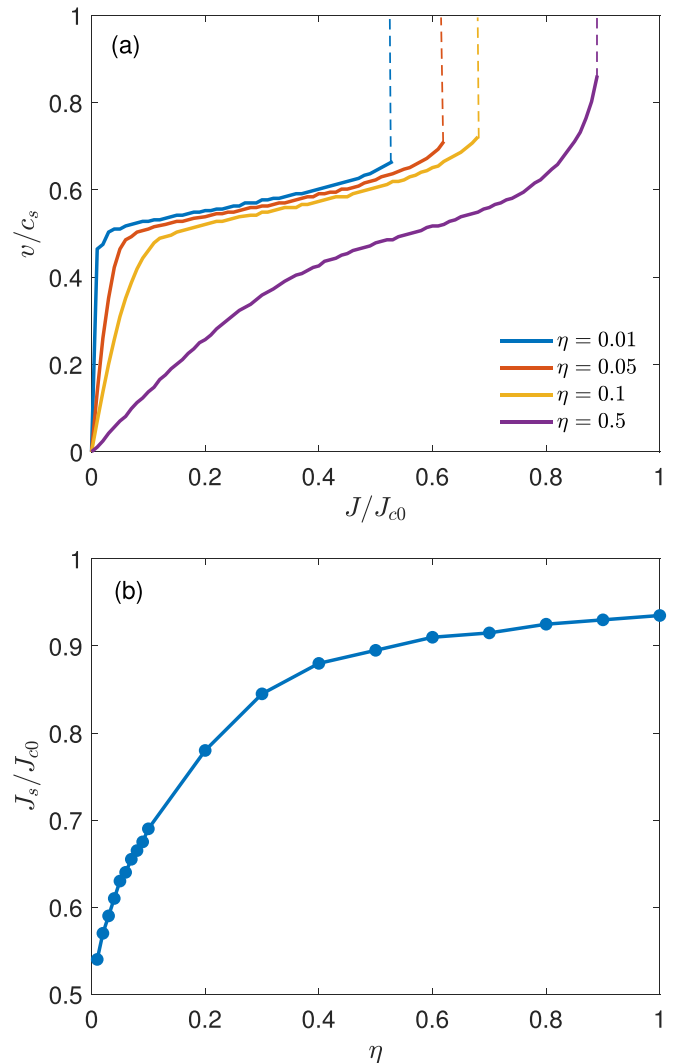


FIG. 4. (a) Stationary velocities of a vortex moving along the central JJ as a function of the bias current at different damping parameters  $\eta$ . (b) The threshold current density  $J_s$  corresponding to the end points of the  $v(\beta)$  curves in (a) as a function of  $\eta$  calculated for  $\zeta = 30962$ .

with a constant dc bias current  $\beta$  through each JJ added in Eq. (1) [44]. Here we adopt a more consistent approach in which  $\beta$  is taken into account through the boundary conditions at the top and the bottom JJ [41–43]. Both approaches produce the same qualitative results.

Dynamics of a vortex in the current-biased JJ stack depends crucially on the damping parameter  $\eta$ . If  $\eta \gtrsim 1$  a vortex initially trapped in a JJ is pushed by current toward the edge of the stack and exits. In an underdamped stack with  $\eta \ll 1$  the vortex colliding with the edge changes polarity and gets reflected as antivortex. This process can also be viewed as a vortex exit followed by penetration of antivortex. The polarity change upon each reflection of the vortex from the edges results in a vortex-antivortex (V-AV) shuttle and temporal oscillations of the magnetic moment  $M(t)$  with the flight frequency  $f_v \simeq v/2L_x$  depending on the vortex velocity  $v$  and the JJ length  $L_x$ . Such oscillations of  $M(t)$  calculated from Eq. (7) are shown in Fig. 2 for a vortex moving along a central

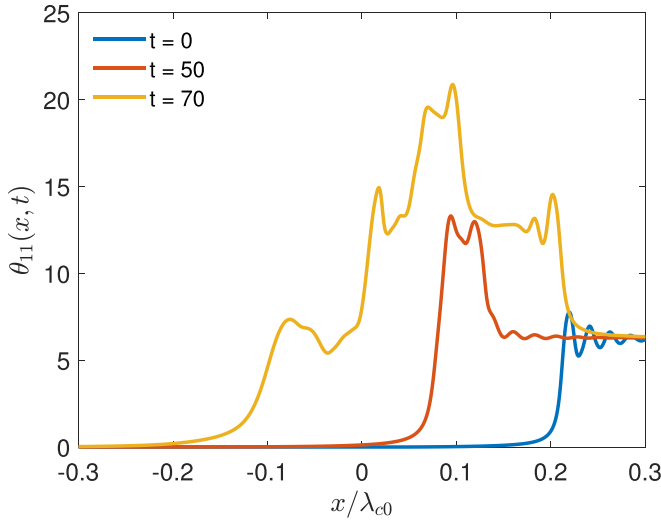


FIG. 5. Snapshots of V-AV pairs generated by a vortex propagating along the central junction in a long stack ( $L_x \gg \lambda_c$ ) calculated at  $\eta = 0.1$  and  $\beta = 0.69$ .

JJ (a) and one trapped vortex per each JJ (b). In both cases we have  $f_v \sim 10^{-2}\omega_{J0}$ . The ripples on  $M(t)$  seen in Fig. 2 result from the bremsstrahlung caused by acceleration of the vortex due to its attraction to the AV image at the edges.

The velocity of the V-AV shuttle is controlled by the balance of the Lorentz force and quasiparticle viscous drag at small currents and by the radiation losses at higher currents [3]. The radiation losses are caused by the trailing Cherenkov wake behind a moving vortex shown in Fig. 3. To see interplay of these mechanisms, consider a vortex propagating uniformly along a long JJ stack. Shown in Fig. 4 is the velocity  $v(\beta)$  of a vortex driven along the central JJ calculated from Eq. (1) without thermal feedback, where  $v(\beta)$  is normalized to  $c_s = cs/\lambda\sqrt{\epsilon_c}$  of the order of the Swihart velocity [3]. The initial steep increase of  $v(\beta)$  controlled by the weak viscous drag is followed by the sharp decrease in the slope of  $v(\beta)$  due to radiation losses. At  $\eta = 0.1$  the radiation-limited velocity  $v \simeq 0.5c_s$  determines the flight frequency  $f_v = v/2L_x$  of the bouncing vortex. For  $L_x = \lambda_{c0}$  used in our simulations,  $f_v \sim (s/\lambda)\omega_{J0} \sim 10^{-2}\omega_{J0}$ , consistent with Fig. 2.

The radiation-controlled parts of  $v(\beta)$  in Fig. 4 are terminated at the end points  $\beta = \beta_s$ . At  $\beta > \beta_s$  the steady-state propagation of the vortex becomes impossible because the Cherenkov wake gets so strong that it causes spontaneous production of V-AV pairs. This process is illustrated by Figs. 3 and 5, which show a Cherenkov wake with  $5\pi/2 < \theta_n < 7\pi/2$  behind the moving vortex. A uniform state with  $5\pi/2 < \theta_n < 7\pi/2$  is unstable with respect to small perturbations  $\delta\theta_n \ll 1$  but gets stabilized in a domain of finite length. As  $\beta$  increases, the amplitude and the width of this domain grow so that at  $\beta = \beta_s$  it becomes unstable and splits, triggering a cascade of expanding V-AV pairs, as shown in Fig. 5. In turn, the Cherenkov wake on the central JJ induces new V-AV pairs on the neighboring JJs. Those V-AV pairs start splitting and propagating both along and across the stack; vortices and antivortices bundle in spatially separated multiquanta flux spots

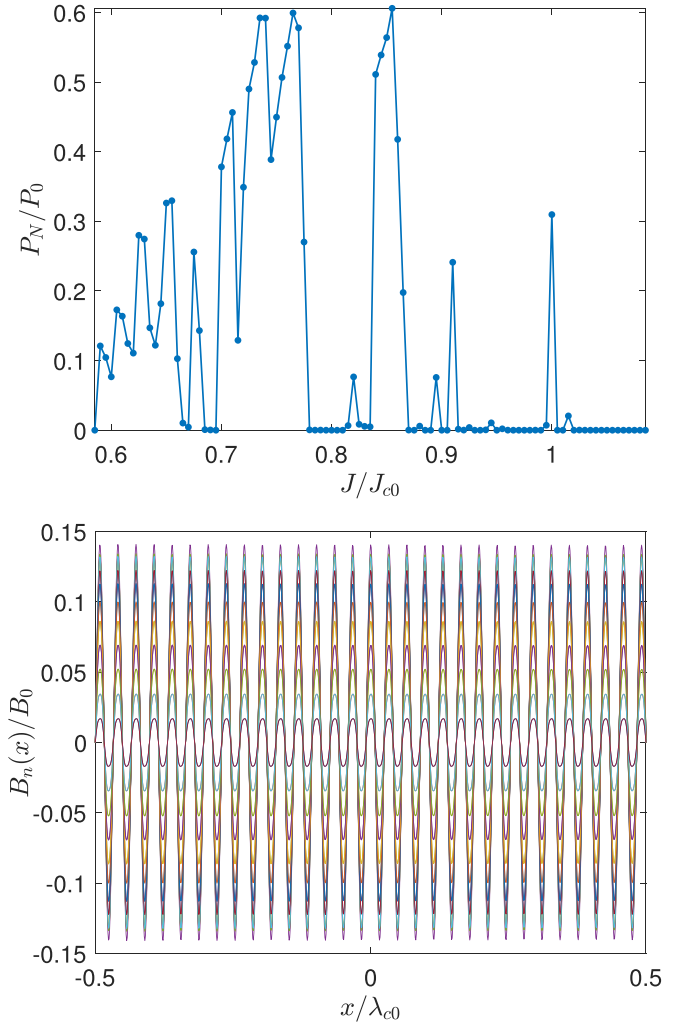


FIG. 6. (Top) Radiated power,  $P_N(\beta)$ , as a function of current calculated for a stack of length  $L_x = \lambda_{c0}$  and  $N = 21$ . (Bottom) Snapshots of a resonant mode in  $B_n(x, t)$  on different JJs at the peak in  $P_N(\beta)$  above at  $\beta = 0.85$ .

(macrovortices) [25] and counterpropagating flux spots with opposite polarity [49]. According to Fig. 4(b), the threshold current density  $J_s(\eta)$  for the V-AV pair production in underdamped JJ stacks can be well below the interlayer  $J_c$ .

Flux spots produced by the V-AV shuttle collide with the edges of the stack and change polarity upon each reflection, as shown in Ref. [49]. After repeated bouncing back and forth, these flux spots get synchronized and form a standing EM wave which can cause temporal oscillations of the magnetic moment of the stack:

$$M(t) = M_0 \sum_n \int_0^{L_x/\lambda_{c0}} b_n(x) dx, \quad (7)$$

where  $M_0 = B_0 s \lambda_c L_y / \mu_0 = \phi_0 L_y / 2\pi \mu_0$ . The oscillations of  $M(t)$  result in radiation from JJ stacks. For stacks much smaller than the EM wavelength, the radiated power can be evaluated in magnetodipole approximation  $P_N =$

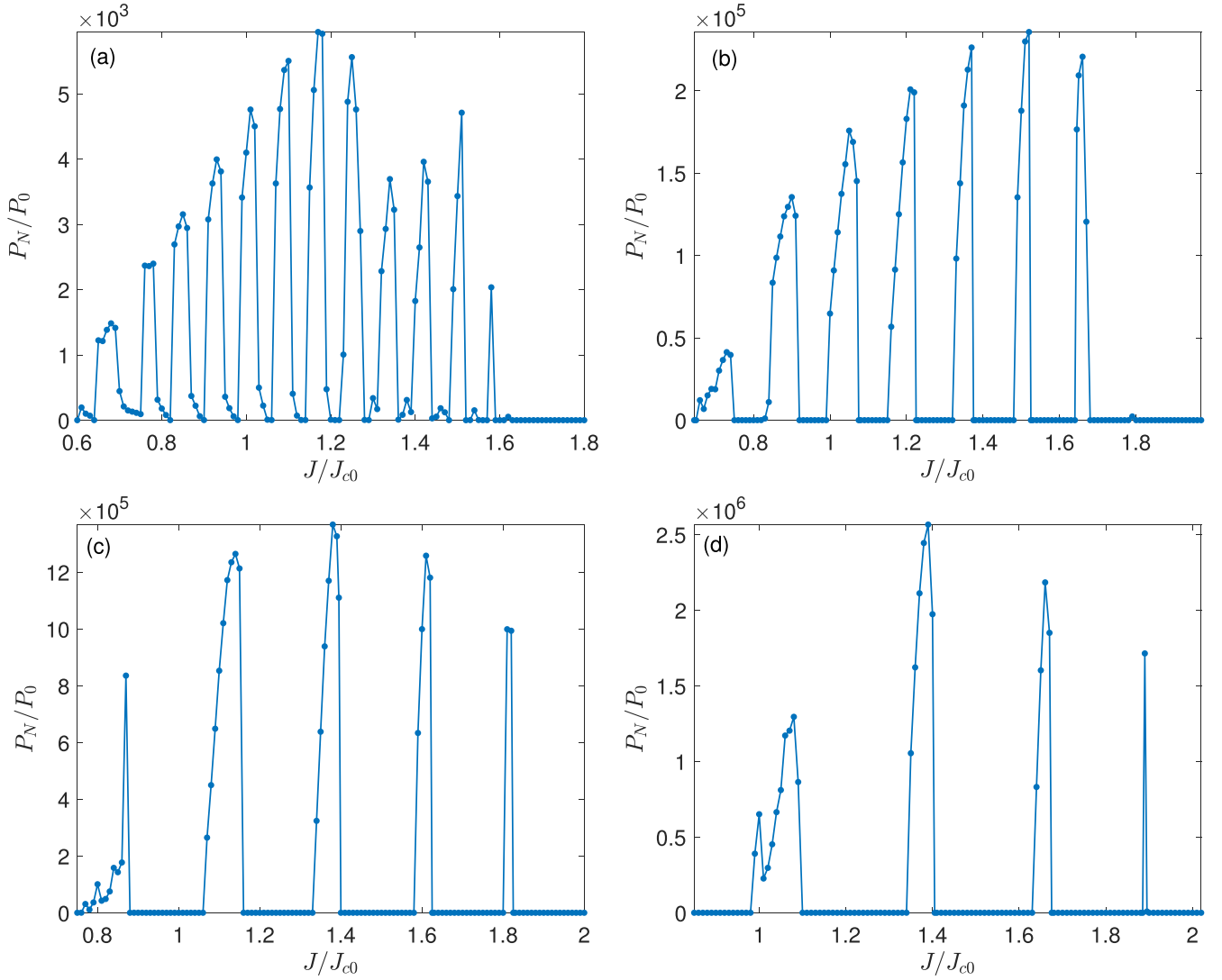


FIG. 7. Radiation power,  $P_N(\beta)$ , calculated for a stack with 81, 161, 261, and 321 JJs as functions of the bias current.

$\mu_0 \langle \dot{M}^2 \rangle / 6\pi c^3$ , where  $\langle \dots \rangle$  denotes time averaging [50]. It is convenient to write  $P_N$  in the form

$$P_N = P_0 G_N, \quad P_0 = \frac{c\phi_0^2 L_y^2}{24\pi^3 \mu_0 \epsilon_c^2 \lambda_c^4}, \quad (8)$$

$$G_N = \int_{t_0}^{t_0+t_a} \left[ \sum_{n=1}^N \int_0^{L_x/\lambda_{c0}} \ddot{b}_n(x, t) dx \right]^2 \frac{dt}{t_a}. \quad (9)$$

Here  $t_0 = 2000$  is chosen to be much larger than a transient time to reach a steady state,  $t_a = 200$  is an averaging time, and  $G_N$  accounts for all harmonics of  $B_n(x, t)$ . For  $L_y = \lambda_c = 295 \mu\text{m}$  and  $\epsilon_c = 12$ , we have  $P_0 \simeq 10^{-13}$  W. Figure 6 shows the calculated  $P_N(\beta)$  which has multiple peaks diminishing at  $\beta \gtrsim 1$ . The peaks in  $P_N(\beta)$  occur at currents for which  $B_n(x, t)$  has odd numbers of half-periods along the stack.

The standing EM wave shown in Fig. 6 is formed by bundles of alternating J vortices and antivortices. The magnitude of  $M(t)$  is proportional to the magnetic flux  $\Phi$  of these bundles; both  $\Phi$  and  $P_N$  increasing strongly with the number  $N$  of JJs in a stack with  $d = sN < 2\lambda$ . This is because the flux of

a J vortex  $\phi$  in a thin stack can be much smaller than  $\phi_0$  [25], similar to the well-known result for the Abrikosov vortex in a thin film [51–54]:

$$\phi(u) = \phi_0 \left[ 1 - \frac{\cosh(u/\lambda)}{\cosh(d/2\lambda)} \right]. \quad (10)$$

Here  $u$  is the distance of the vortex from the center of the stack. The flux  $\phi(u)$  decreases with  $u$  and vanishes at the surfaces  $u = \pm d/2$ , where the vortex is extinguished by its AV image [52,53]. If  $d \ll 2\lambda$ , Eq. (10) gives

$$\phi(u) \simeq \frac{\phi_0 N^2}{8} \left( \frac{s}{\lambda} \right)^2 \left( 1 - \frac{4u^2}{d^2} \right), \quad N \lesssim N_c = \frac{2\lambda}{s}. \quad (11)$$

The reduction of  $\phi(u)$  in a thin stack results from the confinement of vortex currents in a small area  $\sim d^2 \ll \lambda^2$ , which can also be interpreted in terms of partially extinguishing the vortex field by its AV images. For  $N = 21$ ,  $s = 1.5$  nm, and  $\lambda = 264$  nm, we get  $\phi(0) \simeq 1.8 \times 10^{-3} \phi_0$ . At  $N \lesssim N_c$  the flux  $\phi$  is greatly reduced but  $\Phi \sim \phi_0 (N/N_c)^2 N$  of flux spots and  $P_N \propto N^6$  increase rapidly with  $N$ . For  $\lambda(T_0) = 264$  nm and  $s = 1.5$  nm, we obtain  $N_c \simeq 352$  at 4.2 K. Overheating

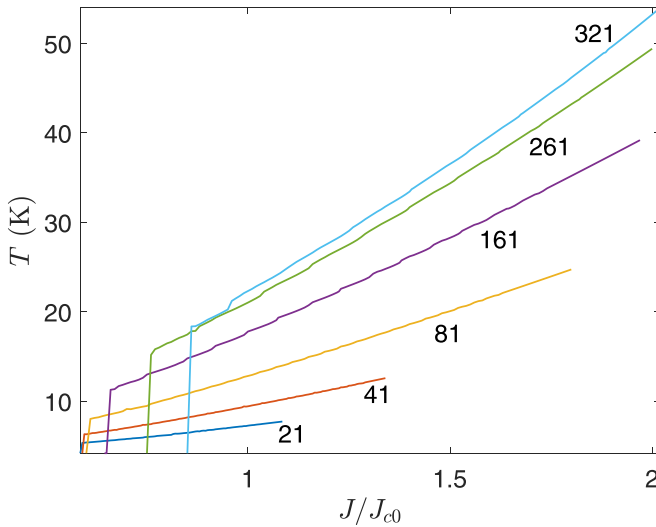


FIG. 8. Mean temperatures  $T(J)$  of JJ stacks with different numbers of layers. The sharp increase of  $T(J)$  occurs at the onset of the V-AV pair production.

increases  $N_c(T)$ ; for instance, at  $T = 50$  K, Eq. (5) yields  $N_c(T) \simeq 440$ .

#### IV. SINGLE VORTEX TRAPPED IN THE CENTRAL JUNCTION

In this section we present numerical results for a dynamic state stimulated by a V-AV shuttle trapped in the central JJ of a stack with  $\eta = 0.1$  [44] and  $21 \leq N \leq 321$ . After the standing EM wave sets in at  $\beta > \beta_s$ , the steady-state  $P_N(\beta)$  and  $T_N(\beta)$  were calculated. The resulting  $P_N(\beta)$  evaluated in the magnetodipole approximation and  $T_N(\beta)$  raise sharply at the current onset of the V-AV pair production  $J_s$ , as shown in Figs. 7 and 8. Here  $J_s(N)$  increases with  $N$  but remains below the interlayer  $J_c$ , as shown in Fig. 9.

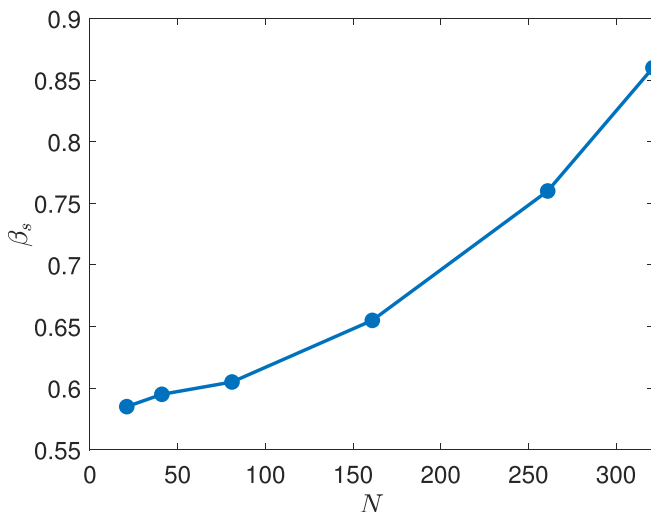


FIG. 9. Current threshold of the V-AV pair production  $\beta_s$  as a function of  $N$ .

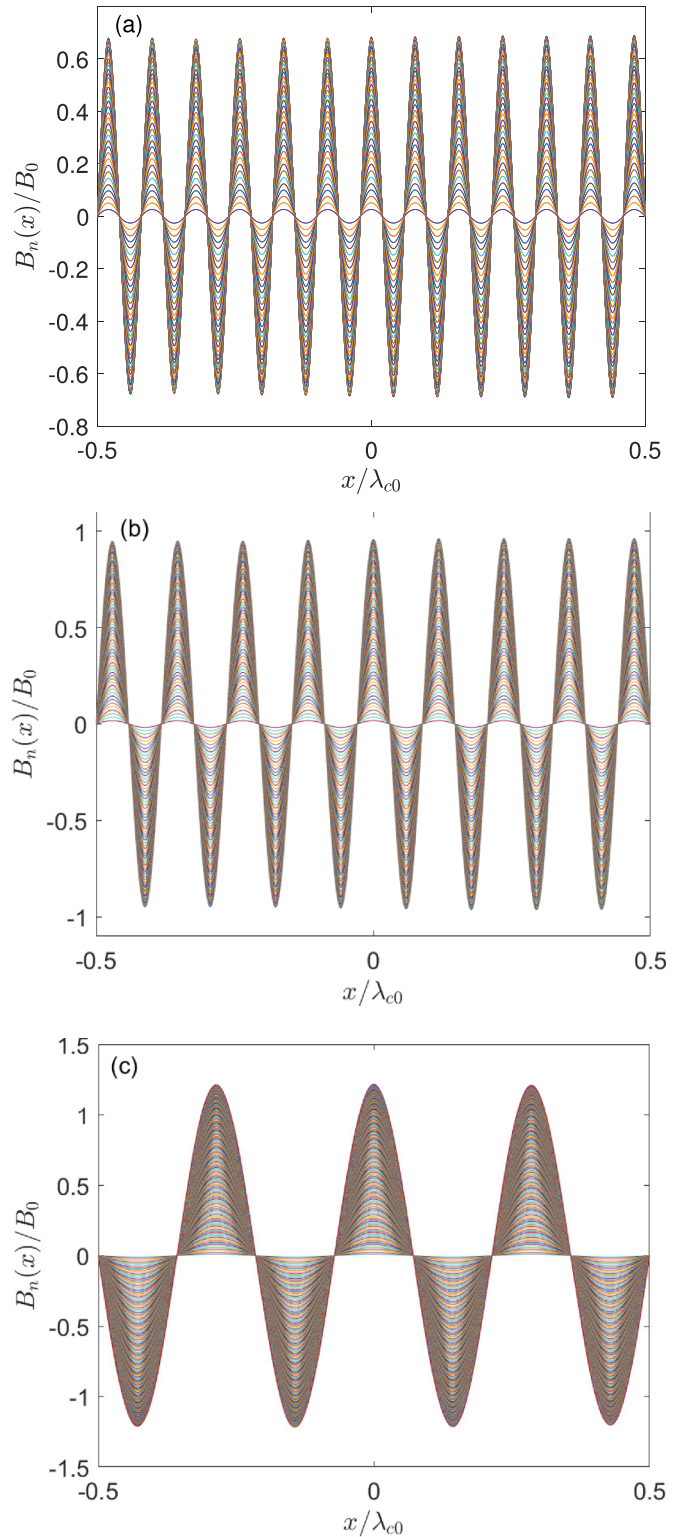


FIG. 10. Snapshots of odd resonant modes in  $B_n(x, t)$  on different layers in a stack with (a)  $N = 81$  at a radiation peak at  $\beta = 1.17$ , (b)  $N = 161$  at a radiation peak at  $\beta = 1.52$ , and (c)  $N = 321$  at the radiation peak at  $\beta = 1.39$ .

The radiated power  $P_N(\beta)$  as a function of current has sharp peaks, whereas  $T(\beta)$  increases smoothly with  $\beta$  after the initial jump at  $\beta = \beta_s$ . The peaks in  $P_N(\beta)$  occur for standing

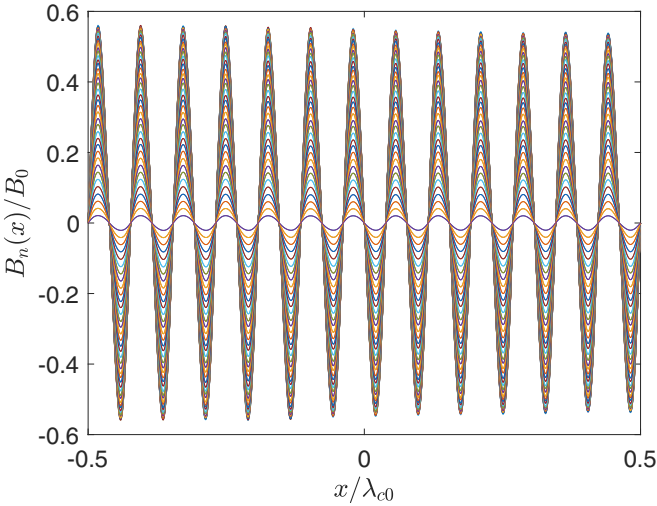


FIG. 11. Snapshot of even mode  $B_n(x, t)$  on different layers at minimum  $P_N(\beta)$  at  $\beta = 1.2$  and  $N = 81$ .

waves in  $B_n(x, t)$  with odd numbers  $m$  of half-periods, as shown in Fig. 10. In turn, the minima in  $P_N(\beta)$  correspond to even numbers  $m$  of half-periods of  $B_n(x, t)$  with about the same amplitudes as for the odd modes (see Fig. 11). The unequal number of positive and negative peaks in  $B_n(x, t)$  with odd  $m$  causes temporal oscillations of  $M(t)$  proportional to the areas of the single peak. The field amplitudes of the strongest resonant mode increase from  $0.14B_0$  at  $N = 21$  to  $1.2B_0$  at  $N = 321$ , where  $B_0 = \phi_0/2\pi s\lambda_{c0}$  is much larger than the lower critical field  $B_{c1} = (\phi_0/4\pi\lambda\lambda_c)[\ln(\lambda/s) + 1.12]$  [55]. The wavelength of the resonant mode at the highest peak in  $P_N(\beta)$  increases with  $N$ , so  $M_N(\beta)$  proportional to the area under the peak in  $B_n(x, t)$  increases strongly with  $N$ , whereas the heights of peaks in  $P_N(\beta)$  first increase with  $\beta$  and then decrease with  $\beta$ . For  $L_y = L_x = \lambda_{c0} = 295 \mu\text{m}$ ,  $\epsilon_c = 12$ , and  $P_0 \simeq 10^{-13} \text{ W}$ , we have  $\tilde{P}_{321} \simeq 0.25 \mu\text{W}$  for a stack with  $N = 321$  at  $\beta \approx 1.4$  according to Fig. 7(d).

### A. Spectral analysis and resonant frequencies

The spectral analysis of  $M_N(\beta, t)$  shows that the standing waves producing the peaks of  $P_N(\beta, t)$  are practically monochromatic; the amplitudes of fundamental harmonics increase strongly with  $N$ . Shown in Fig. 12 are the Fourier spectra of  $\tilde{M}_N(t, \beta)$  for the stacks with  $N = 81$  and 161, where the tilde marks  $\tilde{M}_N(t, \beta)$  and  $P_N(\beta)$  corresponding to the highest peak in  $P_N(\beta)$  with frequencies  $\tilde{f}_N \simeq (1 - 2.2)\omega_{J0}$ . The Fourier spectra of  $\tilde{M}_N(t, \beta)$  also contain small low-frequency harmonics and the third harmonic with amplitude  $\sim 10^{-3}$  of that of the main harmonic. Contributions of the low-frequency and high-frequency harmonics to  $P_N(\beta)$  are negligible.

The EM standing waves shown in Fig. 10 can be described by a subset of eigenmodes in a rectangular JJ stack [39,44,56,57]:

$$B(x, z, t) = B_a \sin\left(\frac{\pi m x}{L_x}\right) \sin\left(\frac{\pi z}{d}\right) e^{-i\omega_m t}. \quad (12)$$

No modes with nodes along  $z$  and  $y$  were observed in our simulations. The frequencies  $f_m = \omega_m/2\pi$  in Eq. (12)

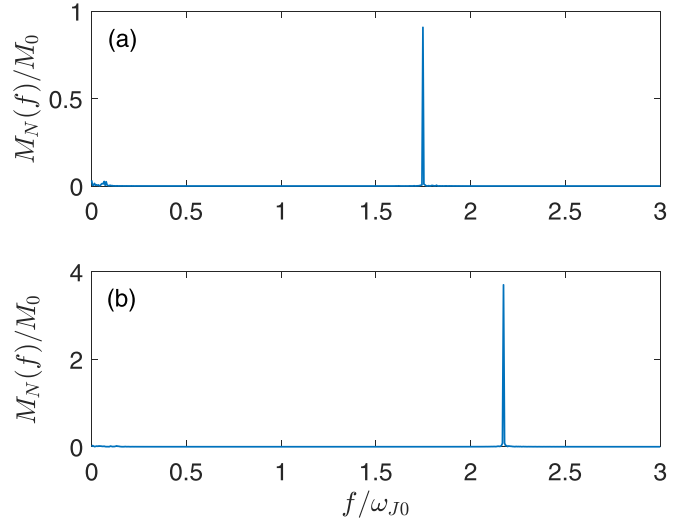


FIG. 12. Fourier spectra of  $M(t)$  at the highest peaks in  $P_N(\beta)$ : (a)  $N = 81$  at  $\beta = 1.17$ ; (b)  $N = 161$  at  $\beta = 1.52$ .

for the modes with  $m$  half-periods obtained from the Fourier spectra are equidistant in odd  $m$ . This is shown in Fig. 13, where each point corresponds to a peak in  $P_N(\beta)$ . The so-obtained  $\omega_m$  match the eigenfrequencies in the inductively coupled JJ stack,  $\omega^2(q_x, q_z) = \omega_J^2 + c_i^2 q_x^2/[1 + 4\zeta \sin^2(sq_z/2)]$  [25,39,44], where  $c_i = c/\sqrt{\epsilon_c}$ ,  $q_x = \pi m/L_x$ ,  $q_z = \pi/d$ , and  $\omega_m \simeq (10 - 14)\omega_J$  (see Figs. 10 and 12). Because  $(\omega_m/\omega_J)^2 \gtrsim 10^2$  and  $sq_z/2 \ll 1$ , the frequencies  $f_m = \omega_m/2\pi$  are equidistant in  $m$  and decrease as the thickness of the stack decreases:

$$f_m = \frac{cm}{2L_x\Gamma}, \quad \Gamma = \sqrt{\epsilon_c[1 + (\pi\lambda/d)^2]}. \quad (13)$$

For  $L_x = \lambda_c$  and  $c_i/\lambda_c = \omega_J$ , we get  $f_m L_x/mc_i = f_m/m\omega_J = 1/2\sqrt{1 + \zeta(\pi/N)^2}$ . The ratios  $f_m L_x/mc_i$  calculated with the account of the dependence of  $\zeta(T)$  on the JJ stack temperature

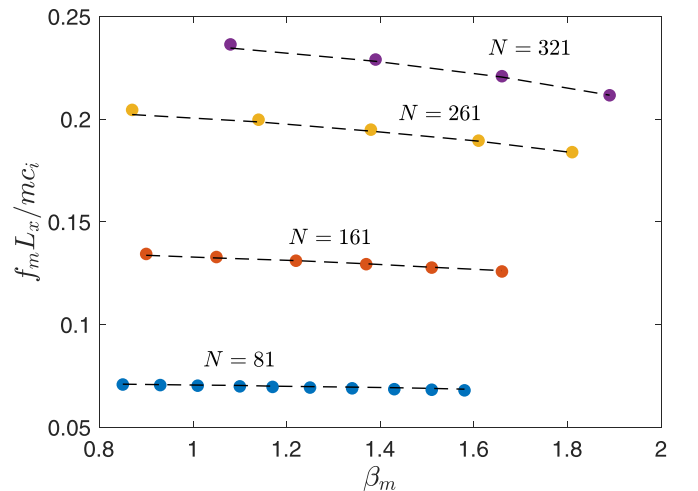


FIG. 13. Ratios  $f_m L_x/mc_i$ , where each data point corresponds to the peaks in  $P_N(\beta)$  corresponding to the standing waves with  $m$  integer half-periods. The dashed lines show  $1/2\sqrt{1 + \zeta(T)(\pi/N)^2}$ .

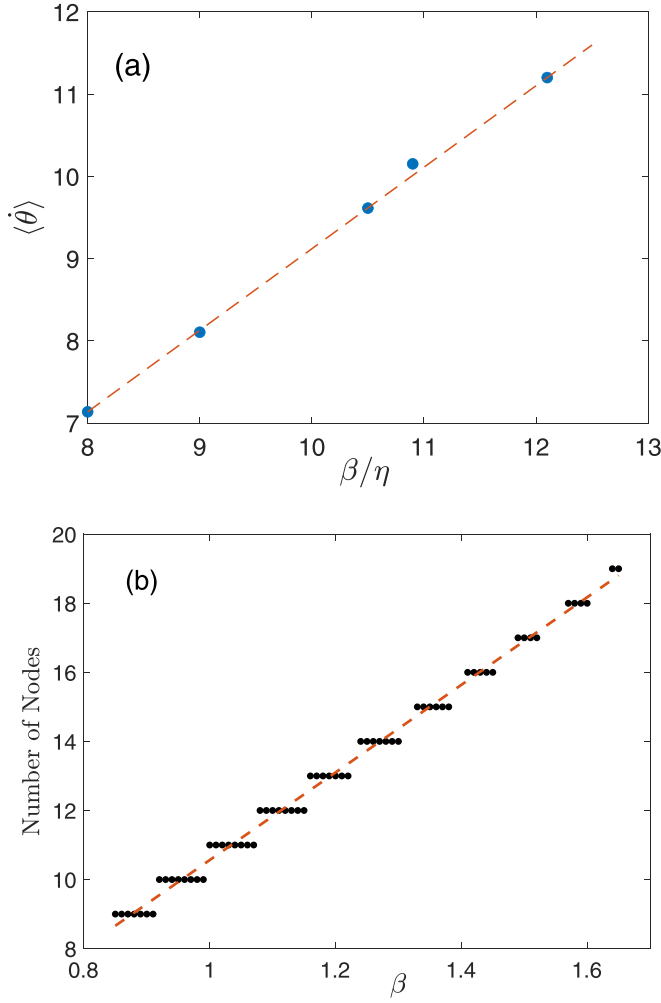


FIG. 14. (a) Mean time derivative of the phase difference  $\langle \dot{\theta} \rangle = \sum_n \int_0^{L_x} \dot{\theta}_n(x, t) dx / NL_x$  in a stack with  $N = 161$ . The dashed line shows  $\dot{\theta} = \beta/\eta$  with  $\eta = 0.1$ . (b) The number of nodes in the resonant modes as a function of  $\beta$  calculated at  $N = 161$ . The dashed line shows  $m = (\beta/\pi\eta)\sqrt{1 + (\pi N_c/2N)^2}$  with  $N_c = 352$  and  $\eta = 0.1$ .

$T(\beta)$  match our numerical data, as shown in Fig. 13. Here a weak decrease of  $f_m L_x / mc_i$  with  $\beta$  results from overheating.

To get more insight into the resonant frequencies, we plot the averaged  $\langle \dot{\theta} \rangle = \sum_n \int_0^{L_x} \dot{\theta}_n(x, t) dx / NL_x$  per JJ at  $N = 161$  in Fig. 14(a), where the dashed line shows  $\dot{\theta}_r = \beta/\eta$ . The good matching of  $\langle \dot{\theta} \rangle$  with  $\beta/\eta$  implies that the dc voltage  $\hbar \langle \dot{\theta} \rangle / 2e$  produced by quasiparticle current causes an oscillating Josephson current  $J_c \sin(\beta t / \eta)$ , which excites a resonance if  $\beta/\eta$  equals one of the mode frequencies  $\pi m / \Gamma$ . The resulting linear relation  $m = \beta \Gamma / \pi \eta$  is consistent with our numerical data shown in Fig. 14(b), where the terraces in  $m(\beta)$  are due to the finite widths of peaks and plateaus in  $P_N(\beta)$ . The resonance condition  $m = \beta \Gamma / \pi \eta$  is equivalent to  $2\pi V / \phi_0 = \pi c m / \Gamma L_x$ , where  $V = Js / \sigma_c$  is the dc voltage per JJ. Such resonances occur at applied voltages  $V_N(m) = \phi_0 c N m / 2L_x \Gamma$  or current densities,

$$J_m = \frac{\phi_0 c \sigma_c m}{2s L_x \Gamma}. \quad (14)$$

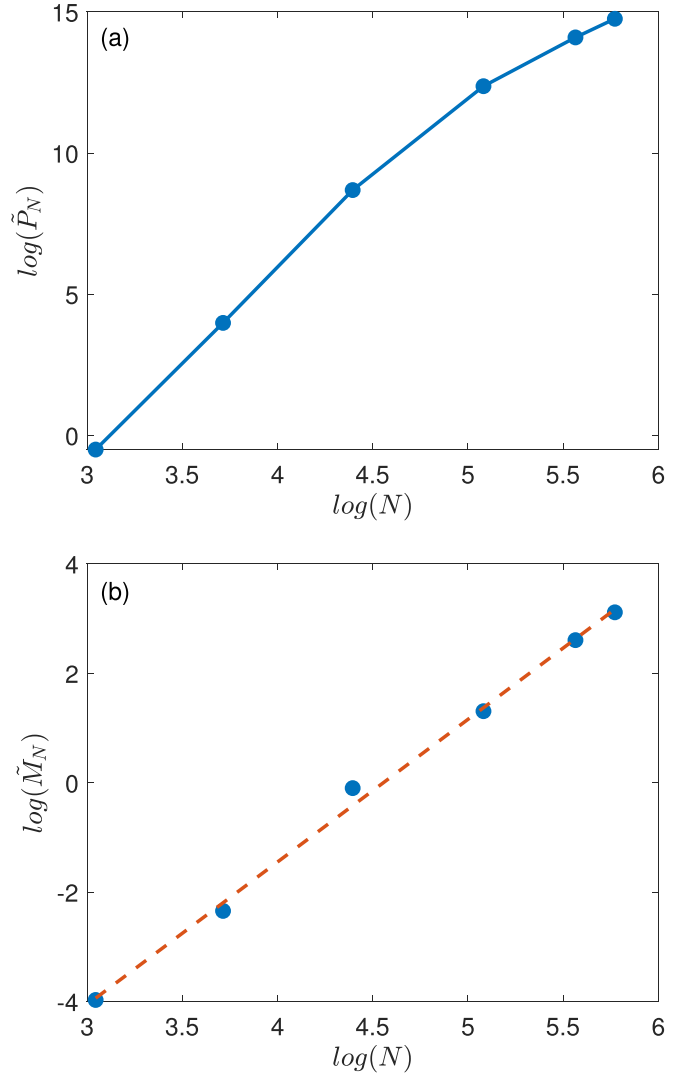


FIG. 15. Log-log plots of the peak radiation power  $\tilde{P}_N$  (a) and the Fourier amplitude  $\tilde{M}_N$  (b) calculated for different numbers of JJ layers in the stack. The dashed line in (b) describes the power law  $\tilde{M}_N \propto N^{2.58}$ .

The magnetic field  $B_n(x, t)$  shown in Figs. 10 and 11 vanishes at the edges of the stack. These modes calculated with the boundary conditions  $\theta'_n(0) = \theta'_n(L_x) = 0$  do not take into account the self-field of transport current. As shown in Appendix C, the self-field of a thin rectangular mesa is much smaller than both the mode amplitudes  $B_a \sim \phi_0 / 2\pi s \lambda_c$  and  $B_{c1}^{\parallel}$ . Equations (12) and (13) are derived in a continuum limit in Appendix D.

## B. Peak radiated power from small stacks

Now we turn to the dependence of the maximum magnetodipole power  $\tilde{P}_N$  on  $N$ , where the tilde marks the highest peak in  $P_N(\beta)$ . Our calculations for  $N = 21, 41$ , and 81 show that  $\tilde{P}_N$  increases as the power law  $\tilde{P}_N \propto N^6$ , which gradually slows down at  $N > 81$ :  $\tilde{P}_{161} \simeq 37\tilde{P}_{81}$ ,  $\tilde{P}_{261} \simeq 6\tilde{P}_{161}$ , and  $\tilde{P}_{321} \simeq 1.85\tilde{P}_{261}$ .

Figure 15 summarizes the dependencies of  $\tilde{P}_N$  and  $\tilde{M}_N$  on the number of JJs. One can see that  $\tilde{P}_N \propto N^6$  persists up



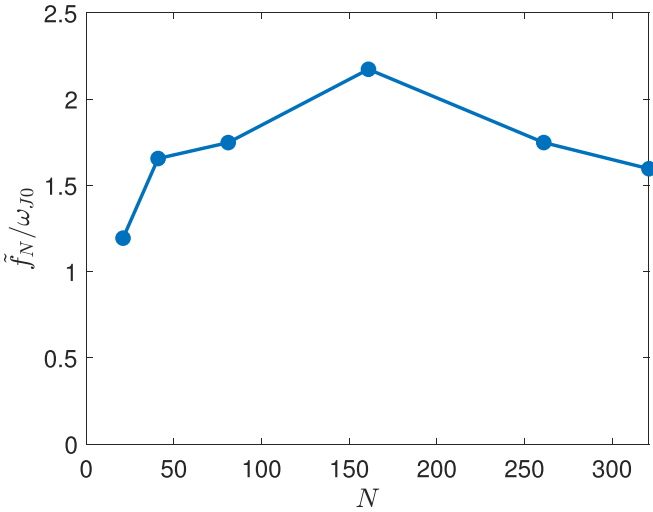


FIG. 16. Resonant frequency  $\tilde{f}_N$  at the highest peaks in the radiated powers as a function of  $N$ .

to  $N = 81$ , while  $\tilde{M}_N \propto N^{2.56}$  persists up to  $N = 321$ . Here  $\tilde{M}_N$  is proportional to the amplitude of magnetic flux in the odd resonant mode  $\Phi = s \sum_n \int B_n(x, t) dx \sim b_m B_0 s N L_x / m$ , where  $m(\beta)$  is the number of nodes and  $b_m(\beta)$  is the amplitude of  $B_n(t)$  in units of  $B_0$ . The behavior of  $\tilde{P}_N$  is determined by the dependencies of  $\tilde{M}_N$  and the corresponding resonance frequency  $\tilde{f}(N)$  on  $N$  shown in Fig. 16. Because of the increase of  $\tilde{f}(N)$  with  $N$  at small  $N$ , the power  $\tilde{P}_N \propto \tilde{M}_N^2 \tilde{f}(N)^4 \propto N^6$  increases faster than  $\tilde{M}_N^2$ , but slows down at  $N > 81$  as  $\tilde{f}(N)$  starts decreasing. Stronger overheating in thicker stacks further slows down the increase of  $\tilde{P}_N$  with  $N$ .

According to Fig. 8, the overheating at  $N \leq 321$  remains moderate and not strong enough to cause a multivalued  $T(\beta)$  necessary for the formation of hotspots [58] in thicker mesas. Yet the decrease of  $J_c(T)$  and  $\omega_J(T)$  with  $T(N)$  diminishes the magnitude and frequency of oscillations of  $M(t)$ . The interplay of the increase of  $M_N$  with  $N$  due to increasing magnetic flux in  $J$  vortices and decrease of  $M_N$  and  $\omega_J(N)$  due to increasing  $T(N)$  as the stack gets thicker can produce a maximum radiation output at an optimum thickness, although it is not yet reached in Fig. 15 as solving Eqs. (1)–(6) with  $N > 321$  becomes very time consuming. There are experimental evidences that the power of THz emission from Bi-2212 mesas increases for thicker Bi-2212 crystals [59].

## V. ONE TRAPPED VORTEX PER JUNCTION

Given that the magnitudes of  $M(t)$  at  $\beta < \beta_s$  increase with the number of trapped vortices [see Fig. 2(b)], one may expect that trapping several vortices could produce stronger excitation of the resonant mode and higher  $P_N(\beta)$ . To investigate this possibility, we solved Eqs. (1)–(6) at  $\eta = 0.1$  with the initial  $\theta_n(x, 0)$  describing a tilted chain of vortices with one vortex per JJ. Simulations show that, after a small current  $\beta \ll 1$  is applied, this vortex configuration buckles and evolves to a nonperiodic structure, consistent with instabilities predicted for vortex structures interacting with a resonant mode in a finite stack [45,60,61]. We observed that few vortices exited

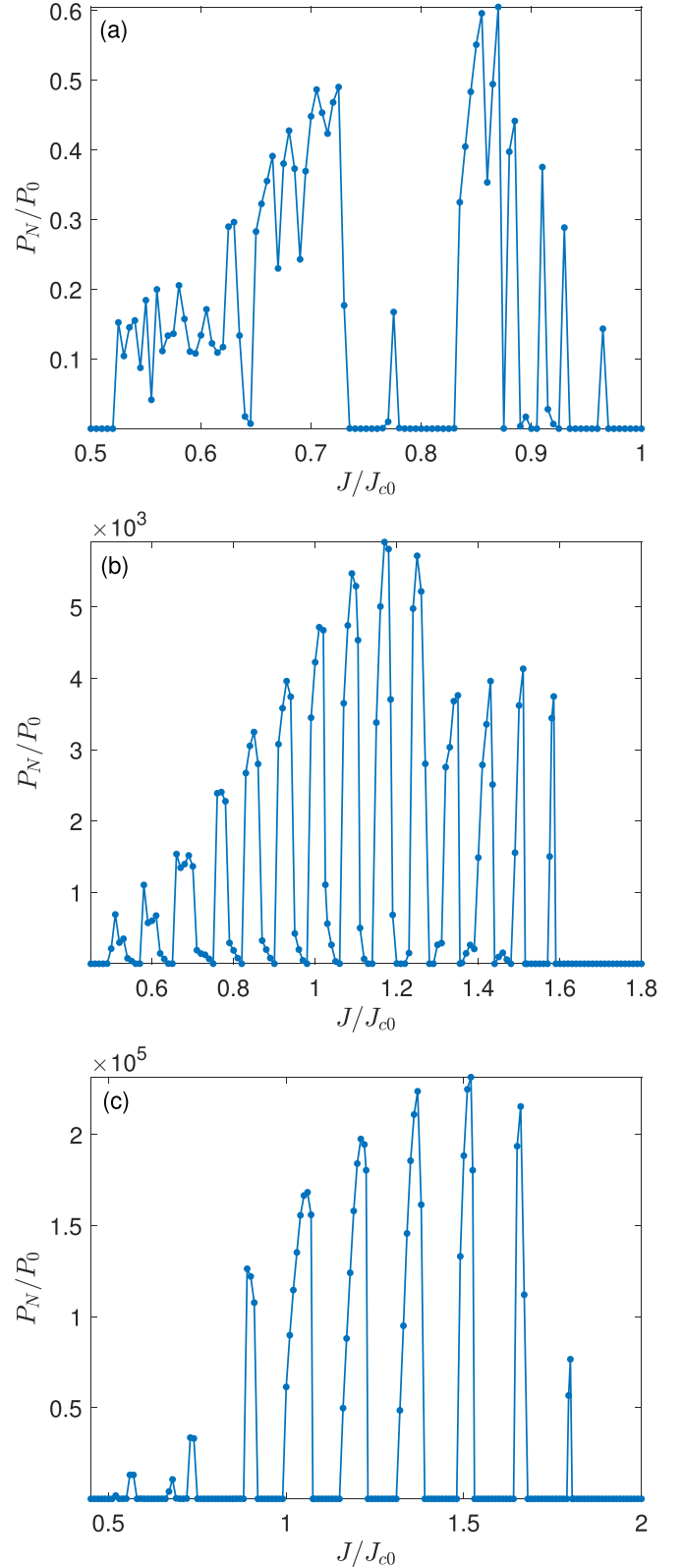


FIG. 17. Radiated power  $P_N(\beta)$  for one trapped vortex per JJ for stacks with (a)  $N = 21$ , (b)  $N = 81$ , and (c)  $N = 161$ .

the stack; some accelerated at the edges producing V-AV pairs similar to that shown in Fig. 5.

As  $I$  is increased, trapped vortices driven along different JJs start producing V-AV pairs in the bulk above different

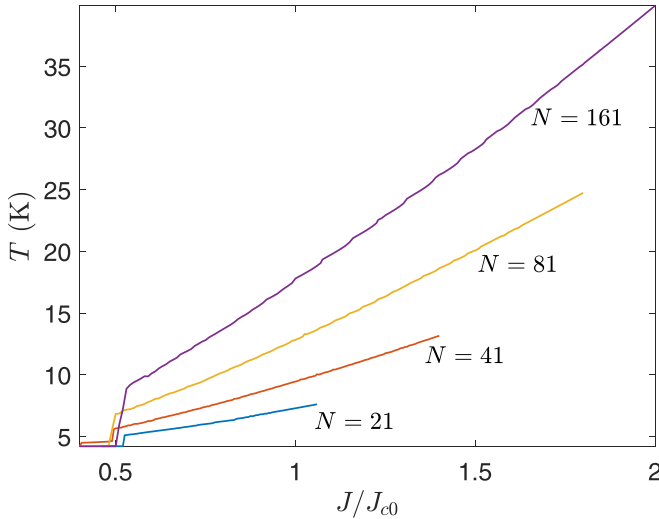


FIG. 18.  $T(J)$  curves for one trapped vortex per JJ for different numbers of layers. The initial jump is smeared out compared to that in Fig. 8.

threshold currents  $\beta_s(n)$  which depend on the positions of JJs in the stack. Here  $\beta_s(n)$  is minimum for the central JJ and increases for JJs being closer to the current leads. This happens because the flux  $\phi(u_n)$  [see Eq. (11)] and the Cherenkov wake in a peripheral vortex is reduced stronger by its AV image than for the vortex in the central JJ. This variation of  $\beta_s(n)$  across the stack and multiple degrees of freedom associated with the relative motion of trapped vortices could hinder the synchronization of JJs. Yet our simulations have shown that the resonant mode stimulated by the V-AV pair production by multiple trapped vortices does occur above a threshold current. Such multivortex simulations are more time consuming than for a single vortex, so we restricted ourselves to the JJ stacks with  $N \leq 161$ .

Figures 17–21 summarize our numerical results for one trapped vortex per JJ. The transition to the synchronized JJs is evident from the strong peaks in  $P_N(\beta)$ , a stepwise increase of the stack temperature  $T_N(\beta)$  above a current threshold, and the snapshots of  $B_n(x, t)$ . The resonant modes  $B_n(x, t)$  are stimulated by the multivortex shuttles in the stack, with the peaks in  $P_N(\beta)$  corresponding to the odd number of nodes, as shown in Fig. 19. The resonant frequencies satisfy Eq. (13) like those shown in Fig. 13 for a single vortex. Yet the number of trapped vortices affects the behavior of  $T_N(\beta)$  and  $P_N(\beta)$ . For instance, the temperature jump in Fig. 18 is broader than in Fig. 8 and the distributions of peaks in  $P_N(\beta)$  in Fig. 17 are clearly different from those in Fig. 7 for a single vortex.

Despite the differences in  $P_N(\beta)$  for the single and multivortex cases, their maximum  $\tilde{P}$  corresponding to the highest peak in  $P_N(\beta)$ , the respective resonance frequencies and overheating temperatures are very close, as one can see by comparing Figs. 12 and 20 and Figs. 15 and 21. Not only did we observe the same power-law dependencies of  $\tilde{P}(N) \propto N^6$  and  $\tilde{M}(N) \propto N^{2.58}$  at  $N \leq 161$ , but also the nearly identical snapshots of  $B_n(x, t)$  shown in Figs. 10 and 19, so that the main characteristics at the maximum radiation output turned out to be independent of the number of trapped vortices.

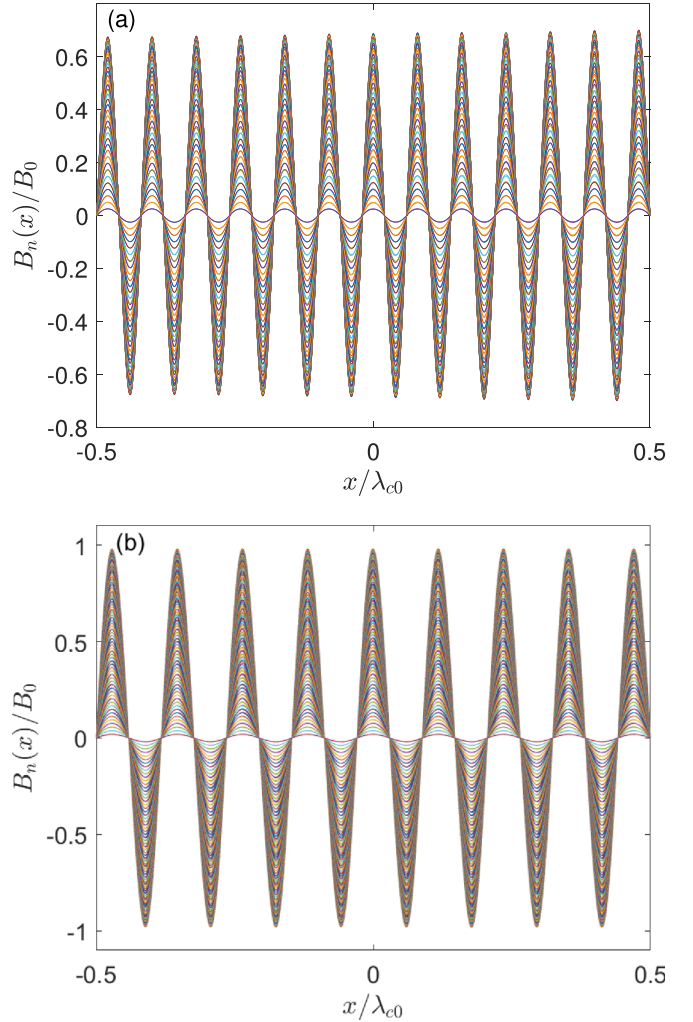


FIG. 19. Snapshots of resonant modes  $B_n(x, t)$  at the maximum radiation power for one trapped vortex per JJ at  $N = 81$  and  $\beta = 1.17$  (top) and  $N = 161$  and  $\beta = 1.52$  (bottom).

## VI. SINGLE-MODE RADIATION

For the parameters  $L_x = \lambda_c \simeq 300 \mu\text{m}$ ,  $\epsilon_c = 12$ , and  $\omega_{J0} = c/\lambda_{c0}\sqrt{\epsilon_c} \simeq 0.3 \text{ THz}$  used in our simulations,  $P_N(\beta)$  is peaked at  $f_m \simeq 2\omega_{J0} \simeq 0.6 \text{ THz}$  (see Fig. 16) and  $\omega_m \simeq 3.8 \text{ THz}$ . The evaluation of  $P_N$  in the dipole approximation captures the qualitative behavior of  $P_N(\beta)$  but is applicable for stacks with  $L_{x,y} \lesssim c/\omega_m \simeq 80 \mu\text{m}$ . Yet we can use our numerical results for  $B_n(x, t)$  valid for any  $L_{x,y}$  to evaluate  $P_N$  produced by single resonant modes defined by Eqs. (12) and (13) in larger stacks with  $L_{x,y} \gtrsim c/\omega_m$ . To do so, we express  $P_N(\beta)$  in terms of the calculated mode amplitude  $B_a$  for a rectangular stack by evaluating the far field single-mode radiation vector potential  $\mathbf{A}(\mathbf{R})e^{-i\omega_m t}$  at large distances  $R \gg k^{-1}$ , where  $k = \omega_m/c$  is the radiation wave vector in free space [50,56]:

$$\mathbf{A}(\mathbf{R}) = \frac{\mu_0 e^{ikR}}{4\pi R} \int_V \mathbf{J}(\mathbf{r}) e^{-ik\mathbf{r}} d^3\mathbf{r}. \quad (15)$$

As shown in Appendix D, the current densities  $J_x(\mathbf{r})e^{-i\omega_m t} = -\mu_0^{-1}\partial B/\partial z$  and  $J_z(\mathbf{r})e^{-i\omega_m t} = \mu_0^{-1}\partial B/\partial x$  in Eq. (15) can be obtained from Eq. (12), where  $J_x$  is determined by in-plane

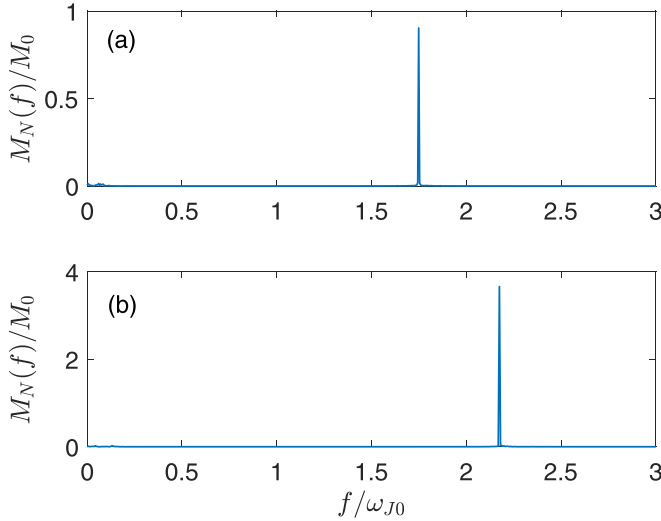


FIG. 20. Fourier spectra of  $M(t)$  at the maximum radiation power for one trapped vortex per JJ and (a)  $N = 81$  at  $\beta = 1.17$  and (b)  $N = 161$  at  $\beta = 1.52$ .

supercurrents and  $J_z$  by polarization currents. In this case the differential radiation power  $dP$  within the solid angle  $d\Omega$  for modes with  $(\omega_m/\omega_J)^2 \gg 1$  and  $\eta \ll 1$  are given by

$$\frac{dP}{d\Omega} = \frac{2cB_a^2L_x^2d^2(k_z^2 + k_x^2)k^2}{\pi^6\mu_0m^2k_y^2} \times \sin^2\left(\frac{k_yL_y}{2}\right) \cos^2\left(\frac{k_xL_x}{2}\right), \quad \text{odd } m, \quad (16)$$

$$\frac{dP}{d\Omega} = \frac{2cB_a^2L_x^2d^2(k_z^2 + k_x^2)k^2}{\pi^6\mu_0m^2k_y^2} \times \sin^2\left(\frac{k_yL_y}{2}\right) \sin^2\left(\frac{k_xL_x}{2}\right), \quad \text{even } m. \quad (17)$$

For small stacks with  $L_{x,y} < c/\omega_m$ , Eqs. (16) and (17) can be expanded in  $k$ , giving the dipole radiation power  $P_o \propto k^4$  at odd  $m$  and quadruple radiation  $P_e \propto k^6 \ll P_o$  at even  $m$ . In spherical coordinates with  $k_y = k \cos \chi$ ,  $k_x = k \sin \chi \cos \varphi$ , and  $k_z = k \sin \chi \sin \varphi$ , the angular dependence of  $dP_o(\chi, \varphi)$  for odd  $m$  becomes

$$\frac{dP_o}{d\chi} = \frac{ck^4L_x^2L_y^2d^2B_a^2}{\pi^5\mu_0m^2} \sin^3 \chi. \quad (18)$$

Integration in Eq. (18) gives the total power:

$$P_o = \frac{4\omega_m^4L_x^2L_y^2d^2B_a^2}{3c^3\pi^5\mu_0m^2} = \frac{\mu_0\langle\ddot{M}^2\rangle}{6\pi c^3}, \quad (19)$$

where  $\langle\ddot{M}^2\rangle = M_a^2\omega^4/2$  and  $\mu_0M_a = L_y \int_0^{L_x} dx \int_0^d dz B(x, z) = 4B_aL_xL_yd/\mu_0\pi^2m$ . Equations (18) and (19) reproduce  $dP/d\Omega$  and  $P$  of magnetodipole radiation used above. Taking  $\omega_m$  and  $\Gamma$  from Eq. (13), we write Eq. (19) in the form

$$P_o = \frac{cN^2\phi_0^2L_y^2m^2b_a^2}{3\pi^3\mu_0L_x^2\lambda_c^2\epsilon_c^2[1 + (\pi N_c/2N)^2]^2}. \quad (20)$$

Here the dimensionless field amplitude  $b_a = B_a/B_0$  with  $B_0 = \phi_0/2\pi s\lambda_{c0}$  and the mode number  $m$  for the highest peak in  $P$

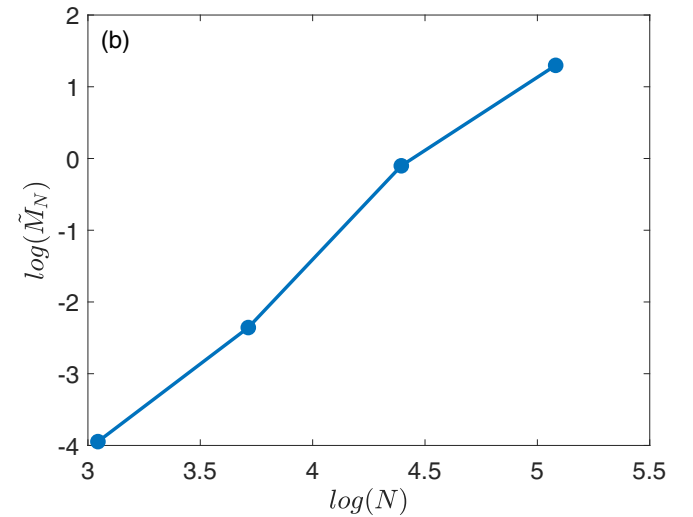
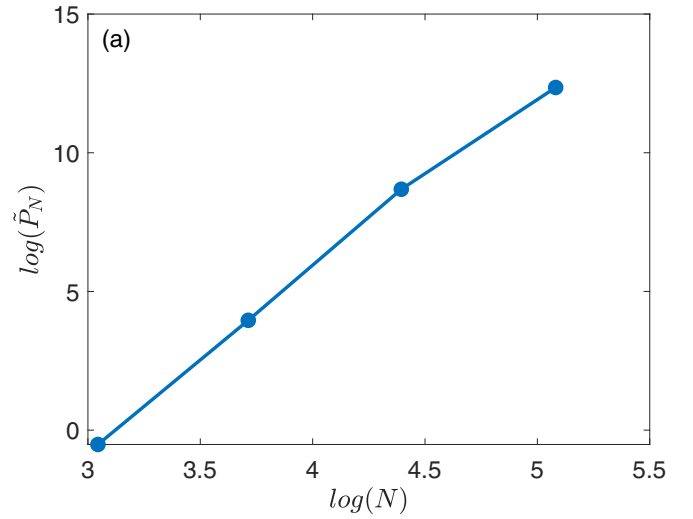


FIG. 21. Log-log plot of the maximum radiation power  $\tilde{P}_N$  (a) and the respective amplitude  $\tilde{M}_N$  (b) versus the number of JJs for one trapped vortex per JJ.

are to be extracted for each  $N$  from the numerical data shown in Fig. 10.

For large stacks with  $kL_y \gg 1$ , not only does the orientational dependence of  $dP(\mathbf{n})/d\Omega$  change, but contributions of even and odd modes become of the same order of magnitude. For instance, Fig. 22 shows markedly different  $P_o(\mathbf{n})$  and  $P_e(\mathbf{n})$  for odd and even modes calculated at  $L_y = 4L_x$  and  $L_x = \lambda_c$ . One can see that  $dP(\mathbf{n})/d\Omega$  along the  $y$  axis gets much smaller than  $dP(\mathbf{n})/d\Omega$  within the  $xz$  plane. This happens in the case of large aspect ratios  $L_y/L_x$  for which the total radiated power can be calculated using that  $\sin^2(k_yL_y/2)/k_y^2$  in Eqs. (16) and (17) is peaked at  $k_y = 0$ , that is,  $\chi = \pi/2$ . Because radiation is mostly confined near the  $xz$  plane, we first evaluate the sheet power  $P_\varphi = \int_0^\pi P(\chi, \varphi) \sin \chi d\chi$  by setting  $\cos \chi \rightarrow u = (\chi - \pi/2) \ll 1$ ,  $\sin \chi \rightarrow 1$ , and using  $\int_{-\infty}^\infty \sin^2(ukL_y/2) du/u^2 = \pi kL_y/2$  to obtain

$$\frac{dP_\varphi}{d\varphi} = \frac{cmL_yd^2B_a^2}{\pi^2\mu_0L_x\Gamma^3} \cos^2\left[\frac{\pi m}{2\Gamma} \cos \varphi\right], \quad \text{odd } m, \quad (21)$$

$$\frac{dP_\varphi}{d\varphi} = \frac{cmL_yd^2B_a^2}{\pi^2\mu_0L_x\Gamma^3} \sin^2\left[\frac{\pi m}{2\Gamma} \cos \varphi\right], \quad \text{even } m. \quad (22)$$

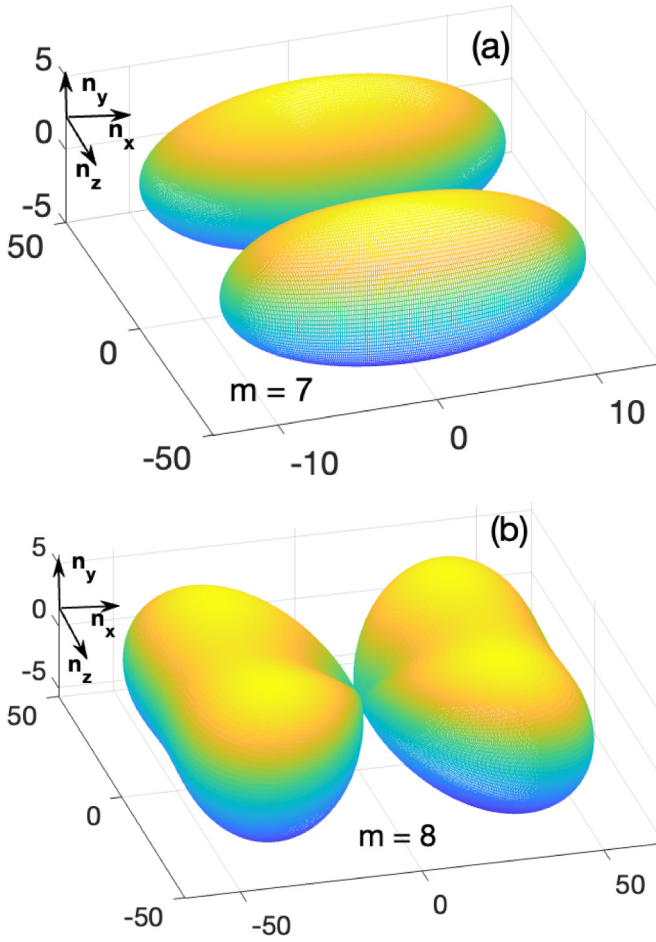


FIG. 22. Angular distribution of the radiation power  $P(\mathbf{n})/P_a$  in the resonant modes with  $m = 7$  (a) and  $m = 8$  (b) calculated from Eqs. (16) and (17) with  $L_x = \lambda_c$  and  $L_y = 4\lambda_c$ . Here  $P_a = 2cB_a^2 d^2 L_x^2 k^2 / \pi^6 \mu_0 m^2$ .

Integration of Eqs. (21) and (22) gives the total power:

$$P_o = \frac{cmL_y d^2 B_a^2}{\pi \mu_0 L_x \Gamma^3} \left[ 1 + J_0\left(\frac{\pi m}{\Gamma}\right) \right], \quad \text{odd } m, \quad (23)$$

$$P_e = \frac{cmL_y d^2 B_a^2}{\pi \mu_0 L_x \Gamma^3} \left[ 1 - J_0\left(\frac{\pi m}{\Gamma}\right) \right], \quad \text{even } m, \quad (24)$$

where  $J_0(x)$  is a Bessel function. As  $\pi m/\Gamma$  increases,  $P_o$  and  $P_e$  oscillate, approaching the common factor  $P_\infty = cmL_y d^2 B_a^2 / \pi \mu_0 L_x \Gamma^3$ , which can be written in the form

$$P_\infty = \frac{cN^2 \phi_0^2 L_y m b_a^2}{4\pi^3 \mu_0 L_x \lambda_{c0}^2 \epsilon_c^{3/2} [1 + (\pi N_c / 2N)^2]^{3/2}}. \quad (25)$$

At  $\pi m/\Gamma \ll 1$  we have  $P_o \rightarrow 2P_\infty$  and  $P_e \rightarrow \pi^2 m^2 P_\infty / 4\Gamma^2 \ll P_o$ , but  $P_e$  can exceed  $P_o$  if  $\pi m/\Gamma > 1$ . For instance, if  $\epsilon_c = 12$ ,  $N = 321$ , and  $N_c = 352$ , we have  $\Gamma = 6.9$ ,  $P_o(m=7) \approx 0.68P_\infty(m)$ , and  $P_e(m=8) \approx 1.4P_\infty(m)$ . From Eqs. (20) and (25), it follows that the power radiation scale  $P_\infty$  from large mesas differs from  $P_o$  for small mesas by a factor  $\sim (kL_y)^{-1} \simeq L_x \Gamma / mL_y$ .

To see how  $P_o$  and  $P_e$  in Eqs. (23) and (24) depend on the mode numbers  $m$ , we also need the dependencies of  $B_a$  on  $m$  to be obtained from the numerical solution of Eqs. (1) and (2).

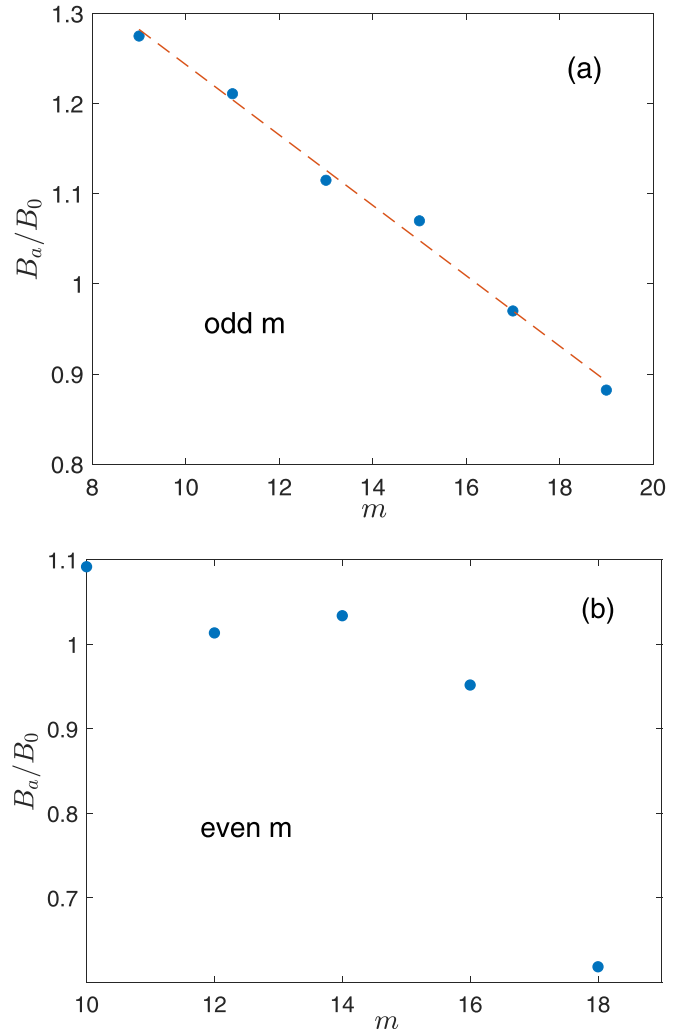


FIG. 23. Amplitudes of resonant modes as a function of the node number  $m$  at  $N = 161$ . Here  $B_a(m)$  for odd modes is calculated at the radiation peaks and  $B_a(m)$  for even modes is calculated at the middle of the plateaus in  $P_N(\beta)$ .

Such  $B_a(m)$  for even and odd modes at  $N = 161$  are shown in Fig. 23. Here  $B_a$  for odd  $m$  was calculated at the peaks of  $P_N(\beta)$  and  $B_a$  for even  $m$  was calculated in the middle of the plateaus in  $P_N(\beta)$  shown in Fig. 7(b). The evaluation of  $B_a$  for even  $m$  is ambiguous as  $B_a$  varies along the plateau. For odd modes,  $b_a \approx 1.32 - 0.038(m - 8)$  decreases linearly with  $m$  so  $mb_a^2$  in Eq. (25) first increases with  $m$ , reaches maximum  $mb_a^2 \approx 16.7$  at  $m = 14$ , and decreases with  $m$  at  $m > 14$ . However, interplay of nonmonotonic  $m$  dependencies of  $mb_a^2$  and  $1 + J_0(\pi m/\Gamma)$  produces an oscillatory  $P_o(m)$  with maxima at  $m = 7$ , and  $m = 23$ , as shown in Fig. 24. The position and the height of the maxima in  $P_o(m)$  depend on the length of the stack,  $L_x$ .

Both Eqs. (20) and (25) give a gradual change of  $P(N)$  from a very rapid increase with  $N$  in thin JJ stacks ( $N \lesssim N_c$ ) to a slower increase of  $P(N)$  in thicker stacks with  $N \gtrsim N_c$ . The products  $m^2 b_a^2$  in Eq. (20) and  $mb_a^2$  in Eq. (25) also depend on  $N$  but they vary much slower than the power laws  $P \propto N^6$  at  $N \lesssim N_c$  and  $P \propto N^2$  at  $N \gtrsim N_c$ . For small mesas,

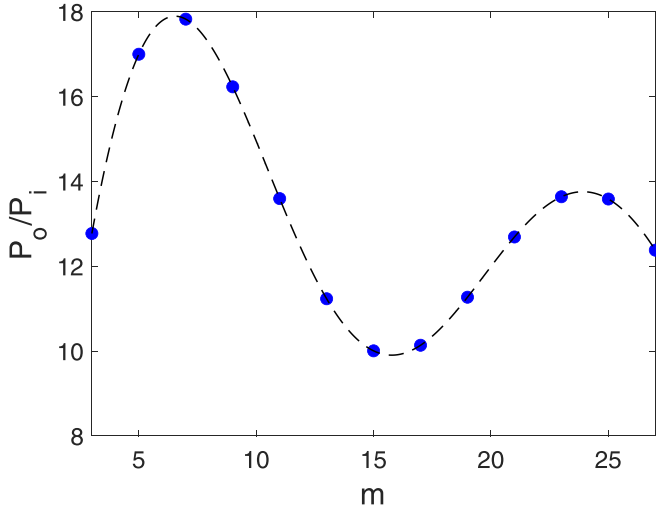


FIG. 24. Radiated power  $P_o(m)$  in units of  $P_i = cL_y d^2 B_0^2 / \pi^2 \mu_0^2 L_x \Gamma^3$  as a function of odd  $m$  calculated from Eq. (23) at  $N = 161$ ,  $\epsilon_c = 12$ , and  $b_a = 1.32 - 0.038(m - 8)$  extrapolated from Fig. 23(a).

$m^2 b_a^2$  varies from 73 to 266 within the range  $21 < N < 321$  in which  $P$  increases by 5–6 orders of magnitude. In larger mesas Eq. (25) suggests a gradual transition from  $P \propto N^5$  at  $N \lesssim N_c$  to  $P \propto N^2$  at  $N \gtrsim N_c$ . Here the product  $mb_a^2$  extracted from the numerical data shown in Fig. 10 varies within the range 10–14 as  $N$  increases from 81 to 321. Another source of  $N$  dependence of  $P_\infty$  comes from overheating, which increases  $\lambda_c(T)$  and  $N_c(T)$ .

## VII. DISCUSSION

This work shows that the bouncing vortex trapped in a layered superconductor can stimulate the V-AV pair production and resonant modes of the JJ stack at a subcritical dc current  $I_s < I_c$ . The giant amplification of the radiation power at  $N \gg 1$  comes from several effects. First, the explosive V-AV pair production caused by Cherenkov instability of the vortex shuttle with low bouncing frequency  $f_v \sim (s\lambda_c/\lambda L_x)\omega_J$  excites resonant modes of the JJ stack with frequencies  $f_m \sim \omega_J \lambda_c m / L_x$  some 2–3 orders of magnitude higher than  $f_v$ . This increases the radiation power by the factor  $\sim (f_m/f_v)^4 \sim 10^8 - 10^{12}$ . Furthermore, the amplitude of magnetic oscillations increases very rapidly with the number of layers due to better synchronization of JJs caused by the increase of the magnetic flux in  $J$  vortices and the number of produced V-AV pairs at  $N \lesssim 2\lambda(T)/s \sim 300 - 500$ .

Our simulations of up to 321 junctions have shown that resonant modes stimulated by the V-AV shuttle produce peaks in the radiation power  $P_N(J)$  at  $J > J_s$ , yet increasing the number of trapped vortices affects weakly the maximum radiation output and the overheating. To estimate the magnitude of  $P_N(m)$  for the mode with  $m = 7$  in the JJ stack with  $N = 321$  and  $\eta = 0.1$ , we take  $b_a \approx 1.2$  from Fig. 10(c),  $L_y/L_x = 4$ ,  $L_x = \lambda_c = 300 \mu\text{m}$ , and  $\epsilon_c = 12$ . In this case  $P_\infty \simeq 0.4 \mu\text{W}$ . If the factor  $mb_a^2$  remains weakly dependent on  $N$  at  $N > 321$ ,

Eqs. (23)–(25) suggest  $P \sim 10 \mu\text{W}$  in a 2–3  $\mu\text{m}$  thick Bi-2212 mesa. Calculation of the actual radiation output may require taking into account a more complicated boundary condition [62–65] at the edges of the stack instead of  $\theta'_n(0) = \theta'(L_x) = 0$  used here. Given the large impedance mismatch between the JJ stack and the vacuum captured by our boundary conditions, the more consistent boundary condition taking into account matching of incoming and radiated EM waves at the edges may not qualitatively change our results but would require numerical calculations including coupling of the mesa with the surrounding structures [2–6,42–44].

The power  $P_N$  depends essentially on the damping parameter  $\eta(T)$  which is affected by doping [66–68]. Decreasing  $\eta$  by doping would reduce both the onset  $J_s(\eta)$  of V-AV pair production (see Fig. 9) and the currents  $J_m$  of intrinsic resonances given by Eq. (14). At  $\eta \ll 1$  the trapped vortex can excite high-frequency modes with  $m \gg 1$  at  $J = J_s$ , thus increasing  $P_N$  as compared to  $P_N$  calculated here for  $\eta = 0.1$  and stimulating THz emission at subcritical currents at which overheating is reduced. Doping also affects a dissipative contribution of in-plane quasiparticle currents [6,45] neglected in Eqs. (1) and (2). The in-plane damping is most pronounced in optimally doped Bi-2212 [6,16], in which it can increase  $J_s$  and mitigate the V-AV pair production. We consider here the most favorable for the V-AV pair production case of weak interplane damping and negligible in-plane damping which may pertain to underdoped Bi-2212.

Utilizing trapped  $J$  vortices to stimulate THz emission offers an opportunity to optimize the radiation output by tuning the field cooling of the mesa through  $T_c$  in a weak magnetic field. For a thick Bi-2212 crystal with  $d > 2\lambda$ , the parallel lower critical field  $B_{c1}^{\parallel} = (\phi_0/4\pi\lambda\lambda_c)[\ln(\lambda/s) + 1.12] \simeq B_{c1}^{\parallel}(0)(1 - T^2/T_c^2)$  [55] not only vanishes at  $T_c$  but  $B_{c1}^{\parallel}(0) \simeq 0.12 \text{ Oe}$  at  $T \ll T_c$  is below the Earth's magnetic field. Thus, trapping an optimum number of vortices upon cooling the mesa through  $T_c$  requires appropriate screening and alignment of the Earth's field relative to the  $ab$  planes. However,  $B_{c1}^{\parallel}(T)$  at  $T \rightarrow T_c$  exhibits a dimensional crossover from the bulk limit at  $d > 2\lambda(T)$  to a thin film limit at  $d < 2\lambda(T)$  in which a weakly  $T$  dependent  $B_{c1}^{\parallel} \simeq (2\phi_0\lambda/\pi\lambda_c d^2) \ln(d/s)$  can significantly exceed the bulk  $B_{c1}^{\parallel}$  because of the reduction of magnetic flux of the vortex [51–54] (see Appendix C). In thin JJ stacks with  $d < 2\lambda(0)$ , the lower critical field is much higher than the bulk  $B_{c1}^{\parallel}(T)$  at all  $T$ .

THz emission stimulated by trapped Josephson vortices can be affected not only by the magnitude but also by the orientation of the ambient field  $\mathbf{H}$  relative to the  $ab$  planes of Bi-2212 crystals. Good alignment of  $\mathbf{H}$  with the  $ab$  planes may be essential to mitigate detrimental penetration of pancake vortices which could deteriorate synchronization of the intrinsic JJs.

## ACKNOWLEDGMENTS

This work was supported by DOE under Grant No. DE-SC0010081-020 and by the AFOSR under Grant No. FA9550-17-1-0196.

### APPENDIX A: MATRIX FORM OF EQ. (1) AND THE BOUNDARY CONDITIONS

The current density across the  $n$ th Josephson junction between the  $(n-1)$ th and  $n$ th superconducting layers is given by

$$J_n^z = \alpha_J(T) \sin \theta_n + \eta \dot{\theta}_n + \ddot{\theta}_n. \quad (\text{A1})$$

In turn, the Maxwell equations give [40–43]

$$\theta_n'' = J_n^z - \zeta(T)(J_{n+1}^z - 2J_n^z + J_{n-1}^z). \quad (\text{A2})$$

Combining Eqs. (A1) and (A2) results in Eq. (1).

For the mesa geometry shown in Fig. 1,  $J_{n-1}^z$  and  $J_{n+1}^z$  for the top and the bottom junctions, respectively, is replaced with the injected dc current density  $J$ . Then Eqs. (A1) and (A2) reduce to the matrix form

$$\Theta'' - \mathbf{V} = \mathbf{A} \cdot (\mathbf{J}^z - \mathbf{V}), \quad (\text{A3})$$

where  $\Theta = (\theta_1, \theta_2, \dots, \theta_N)$ ,  $\mathbf{V} = \beta(1, 1, \dots, 1)$ , and  $\mathbf{J}^z = (J_1^z, J_2^z, \dots, J_N^z)$ . The matrix  $\mathbf{A}$  is given by  $A_{i,i} = 1 + 2\zeta(T)$ ,  $A_{i,i+1} = A_{i,i-1} = -\zeta(T)$ , and  $A_{i,j} = 0$  otherwise. The resulting equations were solved by the method of lines [46] which turns the partial differential Eq. (A3) into a set of ordinary differential equations in time.

### APPENDIX B: HEAT TRANSFER ACROSS THE MESA

For a thin mesa situated at  $0 < z < d \ll w$  on a slab of thickness  $w$  along  $z$  and length  $L_x$  along  $x$ , the thermal diffusion equation is

$$C \partial_t T = \partial_x(\kappa \partial_x T) + \partial_z(\kappa_c \partial_z T) + Q(T)\delta(z), \quad (\text{B1})$$

$$\partial_x T|_{x=0} = \partial_x T|_{x=L_x} = 0, \quad (\text{B2})$$

where  $C(T)$  is the specific heat,  $\kappa_{\alpha\beta}(T)$  is a thermal conductivity tensor with the principal values  $\kappa$  and  $\kappa_c$  in a uniaxial crystal with  $c \parallel z$ , and  $Q(T)$  is the power dissipated in the mesa with thermally insulated sides.

A mean temperature  $T_m$  along the mesa satisfies a stationary equation,  $\partial_z(\kappa_c \partial_z T) + Q\delta(z) = 0$ . Integrating this equation gives a constant heat flux  $q = -\kappa_c \partial_z T$  at  $z > 0$ . Hence  $q = \int_0^w \kappa_c \partial_z T dz/w = w^{-1} \int_{T_i}^{T_m} \kappa_c dT$  and the condition  $Q(T_m) = q$  yields the equation for  $T_m$ :

$$\frac{1}{w} \int_{T_i}^{T_m} \kappa_c(T) dT = Q(T_m). \quad (\text{B3})$$

The temperature  $T_i$  at the bottom of the base is determined by the boundary condition:

$$\kappa_c(T_i) \partial_z T|_{z=w} = Y(T_i^n - T_0^n). \quad (\text{B4})$$

Here  $Y$  is inversely proportional to the Kapitza contact thermal resistance  $R_K = (nYT_0^{n-1})^{-1}$  at  $T_i - T_0 \ll T_0$ , resulting in a temperature jump  $T_i - T_0$  between the base and the sample holder maintained at the ambient temperature  $T_0$ . The exponent  $n$  can vary between 3 and 5, depending on the interface properties [69]. The equation for  $T_i$  readily follows from Eqs. (B3) and (B4):

$$\frac{1}{w} \int_{T_i}^{T_m} \kappa_c(T) dT = Y(T_i^n - T_0^n). \quad (\text{B5})$$

We evaluate the effect of the Kapitza resistance on  $T_m$  at  $T_i - T_0 \ll T_0$  neglecting the temperature dependence of  $\kappa_c(T)$ . Then Eqs. (B3) and (B5) reduce to

$$Q(T_m) = (T_m - T_i)\kappa_c/w, \quad (\text{B6})$$

$$(T_m - T_i)\kappa_c/w = (T_i - T_0)h_K, \quad (\text{B7})$$

where  $h_K = nYT_0^{n-1}$ . Equations (B6) and (B7) yield

$$Q(T_m) = \frac{(T_m - T_0)\kappa_c}{w + \kappa_c/h_K}. \quad (\text{B8})$$

The Kapitza resistance enhances overheating if  $wh_K < \kappa_c$ . The magnitude of  $h_K$  depends on many poorly understood factors including the effect of the Bi-2212 layered structure on the acoustic mismatch of the base and the substrate and details of atomic structure of the interface [69]. Typically  $h_K \sim (1-5) \times 10^4$  W/m<sup>2</sup>K between a metal and the liquid He at 4.2 K, in which case  $wh_K/\kappa_c \sim 1$  for  $w = 30$   $\mu\text{m}$  and  $\kappa_c = 0.6$  W/mK. Yet because  $h_K \propto T^3$  increases faster with  $T$  than  $\kappa_c \propto T^{0.67}$ , the mesa temperature  $T = 20-40$  K shown in Fig. 8 corresponds to the case  $h_K \gg \kappa_c/w$  in which the Kapitza resistance can be disregarded and Eq. (B3) becomes

$$Q(T_m) = \frac{\kappa_0 T_0}{w(a+1)} \left[ \left( \frac{T_m}{T_0} \right)^{a+1} - 1 \right]. \quad (\text{B9})$$

This equation with  $T_m \rightarrow T$  was used in our calculations.

### APPENDIX C: SELF-FIELD EFFECTS

The in-plane self-field  $H_y$  of a uniform current density  $J$  flowing along  $z$  is given by the Biot-Savart law:

$$H_y(\mathbf{r}) = J \int_V \frac{(x' - x)d^3\mathbf{r}'}{|(x - x')^2 + (y - y')^2 + (z - z')^2|^{3/2}}. \quad (\text{C1})$$

We evaluate  $H_y$  in the middle of the stack left face parallel to the trapped vortex ( $x = 0$ ,  $y = L_y/2$ ,  $z = d/2$ ) by first integrating Eq. (C1) with respect to  $z'$ :

$$H_y = Jd \int_0^{L_x} dx' \int_{-L_y/2}^{L_y/2} \frac{x'dy'}{(x'^2 + y'^2)\sqrt{x'^2 + y'^2 + (d/2)^2}}.$$

The  $y'$  integral is then evaluated at  $L_y \gg L_x$ :

$$\int_{-\infty}^{\infty} \frac{dy'}{(x'^2 + y'^2)\sqrt{(d/2)^2 + x'^2 + y'^2}} = \frac{4}{dx'} \tan^{-1} \frac{d}{2x'}.$$

Hence we obtain  $H_y$  at  $d \ll L_x$ :

$$H_y = 4J \int_0^{L_x} dx' \tan^{-1} \frac{d}{2x'} \simeq 2Jd \left[ \ln \frac{2L_x}{d} + 1 \right]. \quad (\text{C2})$$

This formula defines the scale of the in-plane self-field  $B_i \simeq \mu_0 H_y(0)$  which is to be compared to the field amplitude  $B_a \sim B_0 = \phi_0/2\pi s\lambda_c$  in the resonant modes shown in Fig. 10. Using  $\mu_0 J_c = B_0/\lambda_c$ , we recast  $B_i$  to

$$B_i \simeq 2\beta B_0 \frac{d}{\lambda_c} \left( \ln \frac{2L_x}{d} + 1 \right), \quad (\text{C3})$$

where  $\beta = J/J_c$ . The condition  $B_i \ll B_0$  requires

$$\beta \ll \frac{\lambda_c}{2d[\ln(2L_x/d) + 1]}. \quad (\text{C4})$$

Equation (C4) is satisfied at  $L_x = \lambda_c \gg d$  and  $\beta \sim 1$ .

Compare now the self-field with the in-plane lower critical field  $B_{c1}^{\parallel} = (\phi_0/4\pi\lambda\lambda_c)[\ln(\lambda/s) + 1.12]$  at  $d > \lambda$  [55]. The condition  $B_i < B_{c1}^{\parallel}$  requires

$$\beta < \frac{\lambda_c[\ln(\lambda/s) + 1.12]}{4N\lambda[\ln(2L_x/d) + 1]}, \quad d > 2\lambda. \quad (\text{C5})$$

If  $N > N_c(T) = 2\lambda/s \simeq 300\text{--}500$ , Eq. (C5) may not be satisfied at  $\beta > \beta_s$  so vortices could penetrate as  $\beta$  is increased. This may not significantly affect  $P_N$  given the weak sensitivity of  $P_N$  to the number of trapped vortices.

If  $d < 2\lambda$  the condition  $B_i < B_{c1}^{\parallel}$  is satisfied more easily due to larger  $B_{c1}^{\parallel} \simeq (2\phi_0\lambda/\pi\lambda_c d^2)\ln(d/s)$  in thin films [51–54], where the factor  $\lambda/\lambda_c \ll 1$  accounts for the anisotropy of screening. In this case  $B_i < B_{c1}^{\parallel}$  if

$$\beta \lesssim \frac{2\lambda\lambda_c \ln(d/s)}{Nd^2[\ln(2L_x/d) + 1]}, \quad d < 2\lambda. \quad (\text{C6})$$

This condition is satisfied if  $d = \lambda/2$ ,  $L_x = \lambda_c$ ,  $N = 200$ ,  $\lambda_c/\lambda \sim 10^3$ , and  $\beta \simeq 1$ , so the number of trapped vortices remains constant, as it was assumed in our simulations.

#### APPENDIX D: SINGLE MODE RADIATION

To calculate the far field radiation vector potential in Eq. (15), we express the current density in the mesa  $\mathbf{J}(\mathbf{r})$  in terms of the resonant field  $B$  along  $y$ . Because  $\theta_n(x, t)$  varies slowly over the JJ spacing, we replace the discrete  $\theta_n$  and  $B_n$  with smooth functions  $\theta(x, z, t)$  and  $B(x, z, t)$  satisfying Eqs. (1) and (2) in a continuum limit:

$$\frac{\partial^2 \theta}{\partial x^2} = \left[ 1 - \lambda^2 \frac{\partial^2}{\partial z^2} \right] \left[ \frac{\alpha}{\lambda_c^2} \sin \theta + \mu_0 \sigma_c \frac{\partial \theta}{\partial t} + \frac{\epsilon_c}{c^2} \frac{\partial^2 \theta}{\partial t^2} \right], \quad (\text{D1})$$

$$B - \lambda^2 \frac{\partial^2 B}{\partial z^2} = \frac{\phi_0}{2\pi s} \frac{\partial \theta}{\partial x}. \quad (\text{D2})$$

Here the driving term  $\sin \theta$  oscillating with the frequency  $\beta\omega_J/\eta$  sets the amplitude of the resonant mode calculated numerically. The Josephson and ohmic terms in Eq. (D1) affect weakly the resonant frequencies  $\omega_m \gg \omega_J$  which can be obtained by setting  $\alpha = \sigma_c = 0$ . In this case the eigenfrequencies and eigenfunctions of Eqs. (D1) and (D2) satisfying the boundary conditions  $\partial_x B(0, z) = \partial_x B(L_x, z) = 0$  and  $\theta(x, 0) = \theta(x, d) = 0$  are

$$\omega_m = \frac{\pi m c}{L_x \Gamma}, \quad \Gamma = \sqrt{\epsilon_c [1 + (\pi \lambda / d)^2]}, \quad (\text{D3})$$

$$B = B_a \sin \left( \frac{\pi m x}{L_x} \right) \sin \left( \frac{\pi z}{d} \right) e^{-i\omega_m t}, \quad (\text{D4})$$

$$\theta = -\frac{2B_a s L_x \Gamma^2}{m \phi_0 \epsilon_c} \cos \left( \frac{\pi m x}{L_x} \right) \sin \left( \frac{\pi z}{d} \right) e^{-i\omega_m t}. \quad (\text{D5})$$

The in-plane current density  $J_x$  is dominated by the Meissner current; the displacement current is negligible ( $\omega_m \lambda / c^2 =$

$(\pi m \lambda / \Gamma L_x)^2 \ll 1$ ). In turn,  $J_z$  is dominated by the polarization current  $J_z \simeq (\epsilon_c \hbar / 2e s c^2 \mu_0) \omega_m^2 \theta \sim (\omega_m / \omega_J)^2 J_c \gg J_c$ . Using here  $\theta$  from Eqs. (D3)–(D5), we obtain  $J_z = \partial B / \partial x$ ,  $J_x = -\partial B / \partial z$ , and  $J_y = 0$ , where

$$J_x = -\frac{\pi B_a}{\mu_0 d} \sin \left( \frac{\pi m x}{L_x} \right) \cos \left( \frac{\pi z}{d} \right) e^{-i\omega_m t}, \quad (\text{D6})$$

$$J_z = \frac{\pi m B_a}{\mu_0 L_x} \cos \left( \frac{\pi m x}{L_x} \right) \sin \left( \frac{\pi z}{d} \right) e^{-i\omega_m t}. \quad (\text{D7})$$

In this mode  $\nabla \cdot \mathbf{J} = 0$  so it produces no macroscopic charge densities in the bulk and the surface.

The single-mode radiation vector potential  $\mathbf{A}(\mathbf{k}, R, t)$  is readily obtained from Eqs. (15), (D9), and (D10):

$$A_x = \frac{i\pi B_a m k_z L_x d [(-1)^m e^{-ik_x L_x} - 1]}{2R(k_x^2 L_x^2 - \pi^2 m^2)(\pi^2 - d^2 k_z^2) k_y} \times [1 + e^{-idk_z}] \sin \left( \frac{k_y L_y}{2} \right) e^{-ik_y L_y / 2 + ikR - i\omega_m t}, \quad (\text{D8})$$

$$A_z = -A_y k_y / k_z, \quad A_y = 0, \quad (\text{D9})$$

where  $k = \omega_m / c = \pi m / L_x \Gamma$ . Because  $dk_z \lesssim d\omega_m / c = \pi m d / \Gamma L_x \ll 1$ , we set  $e^{-ik_x d} \rightarrow 1$ .

The differential radiation power  $dP = S(\mathbf{n})R^2 d\Omega$  within the solid angle  $d\Omega$  is determined by the Poynting vector  $\mathbf{S} = c|\mathbf{B}|^2 \mathbf{n} / 2\mu_0$  for the far field  $\mathbf{B} = i\mathbf{k} \times \mathbf{A} = i\hat{x}k_y A_z + i\hat{y}(k_z A_x - k_x A_z) - i\hat{z}k_y A_x$  in a plane EM wave propagating along the unit vector  $\mathbf{n} = \mathbf{k}/k$  [50]:

$$\frac{dP}{d\Omega} = \frac{cR^2}{2\mu_0} [k_y^2 (|A_x|^2 + |A_z|^2) + |k_z A_x - k_x A_z|^2]. \quad (\text{D10})$$

Equations (D8)–(D10) give

$$\frac{dP}{d\Omega} = \frac{2cm^2 L_x^2 d^2 B_a^2 (k_z^2 + k_x^2) k^2}{\pi^2 \mu_0 (k_x^2 L_x^2 - \pi^2 m^2)^2 k_y^2} \times \sin^2 \left( \frac{k_y L_y}{2} \right) \cos^2 \left( \frac{k_x L_x}{2} \right), \quad \text{odd } m, \quad (\text{D11})$$

$$\frac{dP}{d\Omega} = \frac{2cm^2 L_x^2 d^2 B_a^2 (k_z^2 + k_x^2) k^2}{\pi^2 \mu_0 (k_x^2 L_x^2 - \pi^2 m^2)^2 k_y^2} \times \sin^2 \left( \frac{k_y L_y}{2} \right) \sin^2 \left( \frac{k_x L_x}{2} \right), \quad \text{even } m. \quad (\text{D12})$$

In spherical coordinates  $k_x = k \sin \chi \cos \varphi$ ,  $k_y = k \cos \chi$ , and  $k_z = k \sin \chi \sin \varphi$ , the factor  $\pi^2 m^2 - k_x^2 L_x^2$  in the denominators of Eqs. (D11) and (D12) becomes  $\pi^2 m^2 [1 - \Gamma^{-2} \sin^2 \chi \cos^2 \varphi]$ . Because  $k_x^2 L_x^2 \ll \pi^2 m^2$  at  $\Gamma^2 \gtrsim \epsilon_c \gg 1$ , Eqs. (D11) and (D12) reduce to Eqs. (16) and (17).

[1] R. Kleiner and P. Müller, Intrinsic Josephson effect in high- $T_c$  superconductors, *Phys. Rev. B* **49**, 1327 (1994).

[2] S. Savel'ev, V. A. Yampol'skii, A. L. Rakhmanov, and F. Nori, Terahertz Josephson plasma waves in layered superconductors:

Spectrum, generation, nonlinear and quantum phenomena, *Rep. Prog. Phys.* **73**, 026501 (2010).

[3] U. Welp, K. Kadowaki, and R. Kleiner, Superconducting emitters of THz radiation, *Nat. Photon.* **7**, 702 (2013).

- [4] I. Kakeya and H. Wang, Terahertz-wave emission from Bi<sub>2</sub>212 intrinsic Josephson junctions: A review on recent progress, *Supercond. Sci. Technol.* **29**, 073001 (2016).
- [5] T. Kashiwagi, H. Kubo, K. Sakamoto, T. Yuasa, Y. Tanabe, C. Watanabe, T. Tanaka, Y. Komori, R. Ota, G. Kuwano, K. Nakamura, T. Katsuragawa, M. Tsujimoto, T. Yamamoto, R. Yoshizaki, H. Minami, K. Kadowaki, and R. A. Klemm, The present status of high- $T_c$  superconducting terahertz emitters, *Supercond. Sci. Technol.* **30**, 074008 (2017).
- [6] R. Kleiner and H. Wang, Terahertz emission from Bi<sub>2</sub>Sr<sub>2</sub>CaCu<sub>2</sub>O<sub>8+x</sub> intrinsic Josephson junction stacks, *J. Appl. Phys.* **126**, 171101 (2019).
- [7] A. Yurgens, Temperature distribution in a large Bi<sub>2</sub>Sr<sub>2</sub>CaCu<sub>2</sub>O<sub>8+δ</sub> mesa, *Phys. Rev. B* **83**, 184501 (2011).
- [8] H. B. Wang, S. Guénon, B. Gross, J. Yuan, Z. G. Jiang, Y. Y. Zhong, M. Grunzweig, A. Iishi, P. H. Wu, T. Hatano, D. Koelle, and R. Kleiner, Coherent terahertz emission of intrinsic Josephson junction stacks in the hot spot regime, *Phys. Rev. Lett.* **105**, 057002 (2010).
- [9] S. Guenon, M. Grunzweig, B. Gross, J. Yuan, Z. G. Jiang, Y. Y. Zhong, M. Y. Li, A. Iishi, P. H. Wu, T. Hatano, R. G. Mints, E. Goldobin, D. Koelle, H. B. Wang, and R. Kleiner, Interaction of hot spots and terahertz waves in Bi<sub>2</sub>Sr<sub>2</sub>CaCu<sub>2</sub>O<sub>8</sub> intrinsic Josephson junction stacks of various geometry, *Phys. Rev. B* **82**, 214506 (2010).
- [10] B. Gross, S. Guenon, J. Yuan, M. Y. Li, J. Li, A. Ishii, R. G. Mints, T. Hatano, P. H. Wu, D. Koelle, H. B. Wang, and R. Kleiner, Hot-spot formation in stacks of intrinsic Josephson junctions in Bi<sub>2</sub>Sr<sub>2</sub>CaCu<sub>2</sub>O<sub>8</sub>, *Phys. Rev. B* **86**, 094524 (2012).
- [11] T. M. Benseman, A. E. Koshelev, W.-K. Kwok, U. Welp, V. K. Vlasko-Vlasov, K. Kadowaki, H. Minami, and C. Watanabe, Direct imaging of hot spots in Bi<sub>2</sub>Sr<sub>2</sub>CaCu<sub>2</sub>O<sub>8+δ</sub> mesa terahertz sources, *J. Appl. Phys.* **113**, 133902 (2013).
- [12] C. Watanabe, H. Minami, T. Kitamura, K. Asanuma, K. Nakade, T. Yasui, Y. Saiwai, Y. Shibano, T. Yamamoto, T. Kashiwagi, R. A. Klemm, and K. Kadowaki, Influence of the local heating position on the terahertz emission power from high- $T_c$  superconducting Bi<sub>2</sub>Sr<sub>2</sub>CaCu<sub>2</sub>O<sub>8+δ</sub> mesas, *Appl. Phys. Lett.* **106**, 042603 (2015).
- [13] F. Rudau, M. Tsujimoto, B. Gross, T. E. Judd, R. Wieland, E. Goldobin, N. Kinev, J. Yuan, Y. Huang, M. Ji, X. J. Zhou, D. Y. An, A. Ishii, R. G. Mints, P. H. Wu, T. Hatano, H. B. Wang, V. P. Koshelets, D. Koelle, and R. Kleiner, Thermal and electromagnetic properties of Bi<sub>2</sub>Sr<sub>2</sub>CaCu<sub>2</sub>O<sub>8</sub> intrinsic Josephson junction stacks studied via one-dimensional coupled sine-Gordon equations, *Phys. Rev. B* **91**, 104513 (2015).
- [14] L. Y. Hao, M. Ji, J. Yuan, D. Y. An, M. Y. Li, X. J. Zhou, Y. Huang, H. C. Sun, Q. Zhu, F. Rudau, R. Wieland, N. Kinev, J. Li, W. W. Xu, B. B. Jin, J. Chen, T. Hatano, V. P. Koshelets, D. Koelle, R. Kleiner, H. B. Wang, and P. H. Wu, Compact superconducting terahertz source operating in liquid nitrogen, *Phys. Rev. Appl.* **3**, 024006 (2015).
- [15] K. J. Kihlstrom, K. C. Reddy, S. Elghazoly, T. E. Sharma, A. E. Koshelev, U. Welp, Y. Hao, R. Divan, M. Tsujimoto, K. Kadowaki, W.-K. Kwok, and T. M. Benseman, Powerful terahertz emission from a Bi<sub>2</sub>Sr<sub>2</sub>CaCu<sub>2</sub>O<sub>8+δ</sub> mesa operating above 77 K, *Phys. Rev. Appl.* **19**, 034055 (2023).
- [16] T. M. Benseman, K. E. Gray, A. E. Koshelev, W.-K. Kwok, U. Welp, H. Minami, K. Kadowaki, and T. Yamamoto, Powerful terahertz emission from Bi<sub>2</sub>Sr<sub>2</sub>CaCu<sub>2</sub>O<sub>8+x</sub> mesa arrays, *Appl. Phys. Lett.* **103**, 022602 (2013).
- [17] R. Wieland, O. Kizilaslan, N. Kinev, E. Dorsch, S. Guénon, Z. Song, Z. Wei, H. Wang, P. Wu, D. Koelle, V. P. Koshelets, and R. Kleiner, Terahertz emission from mutually synchronized standalone Bi<sub>2</sub>Sr<sub>2</sub>CaCu<sub>2</sub>O<sub>8+x</sub> intrinsic Josephson junction stacks, [arXiv:2405.20742v1](https://arxiv.org/abs/2405.20742v1).
- [18] M. A. Galin, E. A. Borodianskiy, V. V. Kurin, I. A. Shereshevskiy, N. K. Vdovicheva, V. M. Krasnov, and A. M. Klushin, Synchronization of large Josephson-junction arrays by traveling electromagnetic waves, *Phys. Rev. Appl.* **9**, 054032 (2018).
- [19] M. A. Galin, F. Rudau, E. A. Borodianskiy, V. V. Kurin, D. Koelle, R. Kleiner, V. M. Krasnov, and A. M. Klushin, Direct visualization of phase-locking of large Josephson junction arrays by surface electromagnetic waves, *Phys. Rev. Appl.* **14**, 024051 (2020).
- [20] S. Y. Grebenchuk, R. Cattaneo, and V. M. Krasnov, Nonlocal long-range synchronization of planar Josephson-junction arrays, *Phys. Rev. Appl.* **17**, 064032 (2022).
- [21] S. Savel'ev, V. Yampol'skii, A. Rakhmanov, and F. Nori, Generation of tunable terahertz out-of-plane radiation using Josephson vortices in modulated layered superconductors, *Phys. Rev. B* **72**, 144515 (2005).
- [22] A. E. Koshelev and L. N. Bulaevskii, Resonant electromagnetic emission from intrinsic Josephson-junction stacks with laterally modulated Josephson critical current, *Phys. Rev. B* **77**, 014530 (2008).
- [23] A. L. Rakhmanov, S. E. Savel'ev, and F. Nori, Resonant electromagnetic emission from intrinsic Josephson-junction stacks in a magnetic field, *Phys. Rev. B* **79**, 184504 (2009).
- [24] S. Z. Lin and X. Hu, In-plane dissipation as a possible synchronization mechanism for terahertz radiation from intrinsic Josephson junctions of layered superconductors, *Phys. Rev. B* **86**, 054506 (2012).
- [25] A. Sheikhzada and A. Gurevich, Instability of flux flow and production of vortex-antivortex pairs by current-driven Josephson vortices in layered superconductors, *Phys. Rev. B* **99**, 214512 (2019).
- [26] G. Hechtfisher, R. Kleiner, A. V. Ustinov, and P. Müller, Non-Josephson Emission from Intrinsic Junctions in Bi<sub>2</sub>Sr<sub>2</sub>CaCu<sub>2</sub>O<sub>8+y</sub>: Cherenkov radiation by Josephson vortices, *Phys. Rev. Lett.* **79**, 1365 (1997).
- [27] A. Sheikhzada and A. Gurevich, Fragmentation of fast Josephson vortices and breakdown of ordered states by moving topological defects, *Sci. Rep.* **5**, 17821 (2015).
- [28] A. Sheikhzada and A. Gurevich, Dynamic transition of vortices into phase slips and generation of vortex-antivortex pairs in thin film Josephson junctions under dc and ac currents, *Phys. Rev. B* **95**, 214507 (2017).
- [29] E. Goldobin, A. Wallraff, and A. V. Ustinov, Cherenkov radiation from fluxon in a stack of coupled long Josephson junctions, *J. Low Temp. Phys.* **119**, 589 (2000).
- [30] E. Goldobin, B. A. Malomed, and A. V. Ustinov, Maximum velocity of a fluxon in a stack of coupled Josephson junctions, *Phys. Lett. A* **266**, 67 (2000).



- [31] E. Goldobin, B. A. Malomed, and A. V. Ustinov, Bunching of fluxons by Cherenkov radiation in Josephson multilayers, *Phys. Rev. B* **62**, 1414 (2000).
- [32] C. Gorria, P. L. Christiansen, Y. B. Gaididei, V. Muto, N. F. Pedersen, and M. P. Soerensen, Fluxon dynamics in three stacked Josephson junctions, *Phys. Rev. B* **66**, 172503 (2002).
- [33] J. Zitzmann, A. V. Ustinov, M. Levitchev, and S. Sakai, Superrelativistic fluxon in a Josephson multilayer: Experiment and simulations, *Phys. Rev. B* **66**, 064527 (2002).
- [34] P. A. Bobbert, Simulation of vortex motion in underdamped two-dimensional arrays of Josephson junctions, *Phys. Rev. B* **45**, 7540(R) (1992).
- [35] F. Estellés-Duart, M. Ortuño, A. M. Somoza, V. M. Vinokur, and A. Gurevich, Current-driven production of vortex-antivortex pairs in planar Josephson junction arrays and phase cracks in long-range order, *Sci. Rep.* **8**, 15460 (2018).
- [36] M. Peyrard and M. D. Kruskal, Kink dynamics in the highly discrete sine-Gordon system, *Physica D* **14**, 88 (1984).
- [37] O. M. Braun and Y. S. Kivshar, *The Frenkel-Kontorova Model: Concepts, Methods, and Applications* (Springer-Verlag, Berlin, New York, 2004).
- [38] S. Sakai, P. Bodin, and N. F. Pedersen, Fluxons in thin-film superconductor-insulator superlattices, *J. Appl. Phys.* **73**, 2411 (1993).
- [39] R. Kleiner, Two-dimensional resonant modes in stacked Josephson junctions, *Phys. Rev. B* **50**, 6919 (1994).
- [40] L. N. Bulaevskii, M. Zamora, D. Baeriswyl, H. Beck, and J. R. Clem, Time-dependent equations for phase differences and a collective mode in Josephson-coupled layered superconductors, *Phys. Rev. B* **50**, 12831 (1994).
- [41] R. Kleiner, T. Gaber, and G. Hechtfisher, Stacked long Josephson junctions in zero magnetic field: A numerical study of coupled one-dimensional sine-Gordon equations, *Phys. Rev. B* **62**, 4086 (2000).
- [42] M. Machida, T. Koyama, and M. Tachiki, Direct numerical experiments for electromagnetic wave emissions with collective Josephson vortex dynamics, *Physica C* **362**, 16 (2001).
- [43] S. Lin, X. Hu, and M. Tachiki, Computer simulation on terahertz emission from intrinsic Josephson junctions of high- $T_c$  superconductors, *Phys. Rev. B* **77**, 014507 (2008).
- [44] X. Hu and S. Lin, Phase dynamics in a stack of inductively coupled intrinsic Josephson junctions and terahertz electromagnetic radiation, *Supercond. Sci. Technol.* **23**, 053001 (2010).
- [45] S. N. Artemenko and S. V. Remizov, Stability of driven Josephson vortex lattice in layered superconductors revisited, *Phys. Rev. B* **67**, 144516 (2003).
- [46] W. E. Schiesser, *The Numerical Method of Lines: Integration of Partial Differential Equations* (Academic Press, San Diego, 1991).
- [47] L. F. Shampine and M. K. Gordon, *Computer Solution of Ordinary Differential Equations: The Initial Value Problem* (W. H. Freeman, San Francisco, 1975).
- [48] T. Jacobs, S. Sridhar, Q. Li, G. D. Gu, and N. Koshizuka, In-plane and  $c$ -axis microwave penetration depth of  $\text{Bi}_2\text{Sr}_2\text{CaCu}_2\text{O}_{8+\delta}$  crystals, *Phys. Rev. Lett.* **75**, 4516 (1995).
- [49] See Supplemental Material at <http://link.aps.org/supplemental/10.1103/PhysRevB.110.094501> for movies of dynamic vortex states.
- [50] J. D. Jackson, *Classical Electrodynamics*, 3rd ed. (Wiley & Sons, Inc., Hoboken, NJ, 1999).
- [51] A. A. Abrikosov, On the lower critical field of thin layers of superconductors of the second group, *Sov. Phys. JETP* **19**, 988 (1964).
- [52] V. V. Shmidt and G. S. Mkrtchyan, Vortices in type-II superconductors, *Sov. Phys. Usp.* **17**, 170 (1974).
- [53] G. Stejic, A. Gurevich, E. Kadyrov, D. Christen, R. Joynt, and D. C. Larbalestier, Effect of geometry on the critical currents of thin films, *Phys. Rev. B* **49**, 1274 (1994).
- [54] A. K. Geim, S. V. Dubonos, I. V. Grigorieva, K. S. Novoselov, F. M. Peeters, and V. A. Schweigert, Non-quantized penetration of magnetic field in the vortex state of superconductors, *Nature (London)* **407**, 55 (2000).
- [55] J. R. Clem, M. W. Coffey, and Z. Hao, Lower critical field of a Josephson-coupled layer model of high- $T_c$  superconductors, *Phys. Rev. B* **44**, 2732 (1991).
- [56] R. A. Klemm, E. R. LaBerge, D. R. Morley, T. Kashiwagi, M. Tsujimoto, and K. Kadowaki, Cavity mode waves during terahertz radiation from rectangular  $\text{Bi}_2\text{Sr}_2\text{CaCu}_2\text{O}_{8+\delta}$  mesas, *J. Phys.: Condens. Matter* **23**, 025701 (2011).
- [57] S. O. Katterwe and V. M. Krasnov, Temperature dependences of geometrical and velocity-matching resonances in  $\text{Bi}_2\text{Sr}_2\text{CaCu}_2\text{O}_{8+x}$  intrinsic Josephson junctions, *Phys. Rev. B* **84**, 214519 (2011).
- [58] A. V. Gurevich and R. G. Mints, Self-heating in normal metals and superconductors, *Rev. Mod. Phys.* **59**, 941 (1987).
- [59] T. Kashiwagi, T. Yuasa, G. Kuwano, T. Yamamoto, M. Tsujimoto, H. Minami, and K. Kadowaki, Study of radiation characteristics of intrinsic Josephson junction terahertz emitters with different thickness of  $\text{Bi}_2\text{Sr}_2\text{CaCu}_2\text{O}_{8+\delta}$  crystals, *Materials* **14**, 1135 (2021).
- [60] M. Machida, Effects of edge boundaries on Josephson vortices in finite-size layered high- $T_c$  superconductors, *Phys. Rev. Lett.* **96**, 097002 (2006).
- [61] A. E. Koshelev, Alternating dynamic state self-generated by internal resonance in stacks of intrinsic Josephson junctions, *Phys. Rev. B* **78**, 174509 (2008).
- [62] M. Leone, The radiation of a rectangular power-bus structure at multiple cavity-mode resonances, *IEEE Trans. Electromagn. Compat.* **45**, 486 (2003).
- [63] L. N. Bulaevskii and A. E. Koshelev, Radiation from a single Josephson junction into free space due to Josephson oscillations, *Phys. Rev. Lett.* **97**, 267001 (2006).
- [64] R. A. Klemm and K. Kadowaki, Output from a Josephson stimulated terahertz amplified radiation emitter, *J. Phys.: Condens. Matter* **22**, 375701 (2010).
- [65] V. M. Krasnov, Coherent flux-flow emission from stacked Josephson junctions: Nonlocal radiative boundary conditions and the role of geometrical resonances, *Phys. Rev. B* **82**, 134524 (2010).

- [66] M. B. Gaifullin, Y. Matsuda, N. Chikumoto, J. Shimoyama, K. Kishio, and R. Yoshizaki, C-axis superfluid response and quasi-particle damping of underdoped Bi:2212 and Bi:2201, *Phys. Rev. Lett.* **83**, 3928 (1999).
- [67] D. N. Basov and T. Timusk, Electrodynamics of high- $T_c$  superconductors, *Rev. Mod. Phys.* **77**, 721 (2005).
- [68] J. Hwang, T. Timusk, and G. D. Gu, Doping dependent optical properties of  $\text{Bi}_2\text{Sr}_2\text{CaCu}_2\text{O}_{8+\delta}$ , *J. Phys.: Condens. Matter* **19**, 125208 (2007).
- [69] J. Chen, X. Xu, J. Zhou, and B. Li, Interfacial thermal resistance: Past, present, and future, *Rev. Mod. Phys.* **94**, 025002 (2022).